THESIS

A NON-INVASIVE HALL CURRENT DISTRIBUTION MEASUREMENT SYSTEM FOR HALL EFFECT THRUSTERS

Submitted by

Carl Raymond Mullins

Department of Mechanical Engineering

In partial fulfillment of the requirements

For the Degree of Master of Science

Colorado State University

Fort Collins, Colorado

Fall 2015

Masters Committee:

Advisor: John Williams

Patrick Shipman
Azer Yalin

ABSTRACT

A NON-INVASIVE HALL CURRENT DISTRIBTUION MEASUREMENT SYSTEM FOR HALL EFFECT THRUSTERS

A direct, accurate method to measure thrust produced by a Hall Effect thruster on orbit does not currently exist. The ability to calculate produced thrust will enable timely and precise maneuvering of spacecraft—a capability particularly important to satellite formation flying. The means to determine thrust directly is achievable by remotely measuring the magnetic field of the thruster and solving the inverse magnetostatic problem for the Hall current density distribution. For this thesis, the magnetic field was measured by employing an array of eight tunneling magnetoresistive (TMR) sensors capable of milligauss sensitivity when placed in a high background field. The array was positioned outside the channel of a 1.5 kW Colorado State University Hall thruster equipped with a center-mounted electride cathode. In this location, the static magnetic field is approximately 30 Gauss, which is within the linear operating range of the TMR sensors.

Furthermore, the induced field at this distance is greater than tens of milligauss, which is within the sensitivity range of the TMR sensors. Due to the nature of the inverse problem, the induced-field measurements do not provide the Hall current density by a simple inversion; however, a Tikhonov regularization of the induced field along with a non-negativity constraint and a zero boundary condition provides current density distributions. Our system measures the sensor outputs at 2 MHz allowing the determination of the Hall current density distribution as a function of time. These data are shown in contour plots in

sequential frames. The measured ratios between the average Hall current and the discharge current ranged from 0.1 to 10 over a range of operating conditions from 1.3 kW to 2.2 kW. The temporal inverse solution at 2.0 kW exhibited a breathing mode of 37 kHz, which was in agreement with temporal measurements of the discharge current.

ACKNOWLEDGEMENTS

My journey has culminated in great experiences here at CSU. This opportunity would not have been possible without the guidance and support of my advisor, Dr. John D. Williams, whose wisdom, passion for science, and willingness to teach makes this world a better place and has made me a better person. I would also like to express gratitude towards my committee members, Dr. Patrick S. Shipman and Dr. Azer P. Yalin, for their guidance, support, and patience in the completion of this thesis.

I would also like to acknowledge the special contributions of Mr. Rafael A. Martinez, Dr. Casey C. Farnell, and Dr. Cody C. Farnell for their incredible support and assistance in this project that made this research possible. A special thanks goes to Daisy Williams for keeping us all in line, by far one of the more difficult tasks. Acknowledgment is also due for the work done by Dr. Binyamin Rubin and Ms. Zoe Morozko, whose findings paved the way for the work done in this thesis. Thanks is also owed to the Air Force Institute of Technology for their funding and interest in this project as well as the undergraduate researchers at the CEPPE Lab for their time and effort.

I would also like to thank my friends and colleagues here at CSU for their support and company during my time here. I wish you all the best in your future endeavors.

Most importantly I would to thank my parents, Carl and Sandy Mullins, for their unwavering encouragement and support throughout my pursuit for higher education. I aim to repay all the sacrifices you made for me with hard work and success. I love you both.

TABLE OF CONTENTS

LIST OF FIGURES

1. Introduction

This work details the design, development, and utilization of a diagnostic system for Hall thrusters to calculate the Hall current density distribution and thrust. A background on electric propulsion, specifically Hall thrusters, is given in this section and its impact in the aerospace industry is described. The driving factors of performance for a thruster are covered with the last subsection covering several other non-invasive sensor systems that have lead the way to the one presented here in.

1.1 Electric Propulsion

The human endeavor to explore space was first mathematically represented by Tsiolkovsky in the early 20th century when he derived the rocket equation [1]. In this derivation it is clear that maximizing the exhaust velocity of the particles propelled from an engine improves the usable mass. Two major regimes are utilized today for in-space propulsion: chemical and electric-based systems.

Chemical propulsion is commonly used and has a greater history within the space industry. An exothermic chemical reaction between an oxidizer and fuel at high pressures creates high temperatures that, when coupled with a Laval rocket nozzle, accelerate the chemical products away from the spacecraft. These systems are characteristically known for generating large amounts of thrust at the expense of lower I_{sp}, which is defined in Eq. 1, where I represents the total impulse, M_p is the propellant mass, g_e is the acceleration at the surface of the Earth, u_{eq} is the exhaust velocity, T is the thrust, and $\dot{m}$ is the propellant mass flow rate.

$$I_{sp} = \frac{I}{M_p g_e} = \frac{u_{eq}}{g_e} \tag{1-1}$$

$$u_{eq} = \frac{T}{\dot{m}} \tag{1-2}$$

The concept of electric propulsion (EP) has been present since the early 20th century but has only been utilized by the space community in the past few decades. EP systems can be divided into three major subclasses, electrothermal, electrostatic, and electromagnetic. Much like chemical propulsion, electrothermal systems use an electrical arc or resistor to heat gas and accelerate it out of a nozzle. Arcjets and resistojets are examples of this EP class. Electrostatic systems generate electric fields that accelerate ionized particles to high velocities. Ion thrusters are an example of this class and are used significantly for satellite station keeping and more recently for orbit transfer maneuvers[2], [3]. Another example is Hall effect thrusters (HETs), which were initially developed and then abandoned by the US in the 1960's and continuously developed in the USSR and Russia since the 1960's [4]. Electromagnetic thrusters still accelerate ionized particles using electric fields, but they also utilize magnetic fields in the acceleration process. Examples of this subclass consist of high impulse magnetoplasmadynamic thrusters and pulsed plasma thrusters. EP systems typically need less propellant mass and accelerate the ejected particles to much higher velocities compared to chemical propulsion. The focus of this work utilizes a 1.5 kW HET that operates at a specific impulse of ~1600 sec.

1.2 Hall Effect Thruster Operation

The details of HETs and their operation have been covered in previous work [4]–[6]. The Hall thruster was originally conceived from work with cross-field plasma sources and

magnetrons. The pursuit of ion thruster technology in the U.S., coupled with a Russian interest in Hall thrusters, led to HET technology being initially advanced in the Soviet Union. In recent years the desire for higher thrust-to-power EP systems has become apparent [7]. HETs also exhibit the ability to operate over a wide range of power conditions for a fixed design [8].

The basic components of a stationary plasma thruster (SPT) style HET are shown in Figure 1.1, which include an annular discharge channel with a gas distributor, anode, and magnetic circuit. The channel is made of a dielectric material such as boron nitride or borosil. The gas distributor sits in the upstream section of the channel with the purpose of uniformly distributing gas atoms throughout the channel. The anode is located in the same vicinity of the gas distributor, and in some designs the distributor is purposed as the anode as well. A hollow cathode is mounted outside of the channel on the outer radial edge of the thruster and provides electrons to the HET. Modern systems also incorporate a hollow cathode into the center pole of the thruster. The cathode acts to provide electrons for the ionization of the gas and neutralization of the accelerated ions. The discharge supply biases the anode positive relative to the cathode. This creates an axial electric field within the channel near the downstream end.

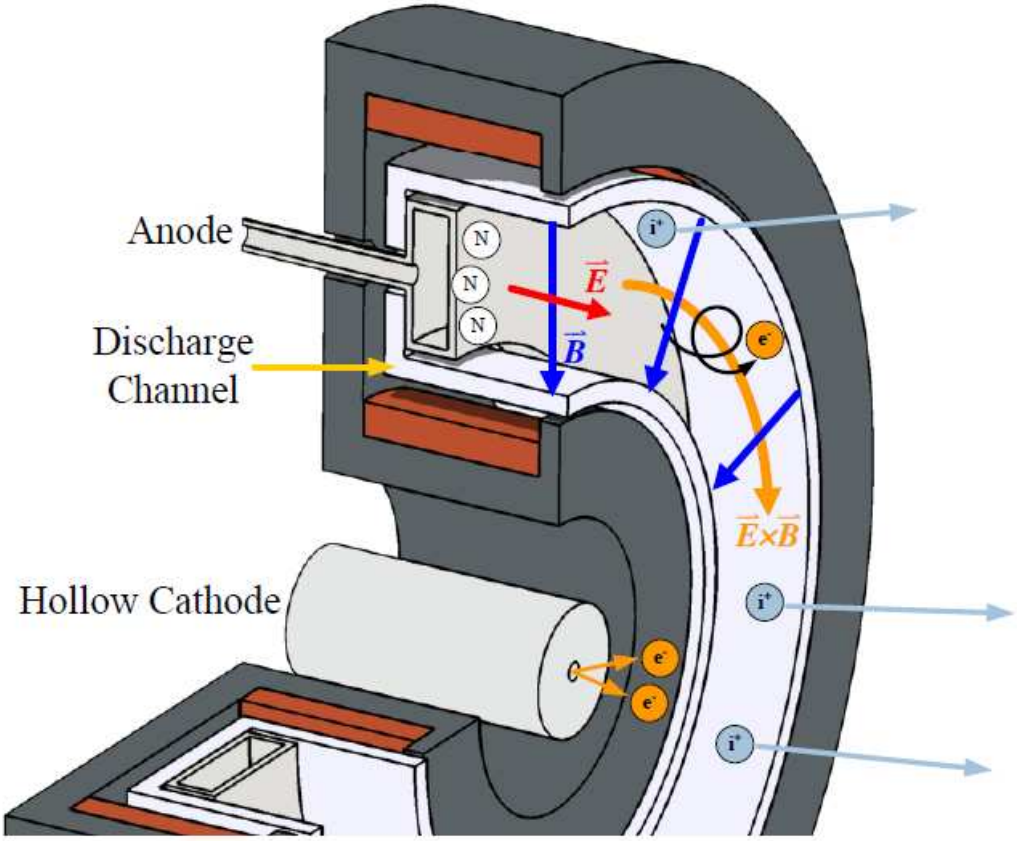

Figure 1.1: Section of a center-mounted HET showing the flow of neutrals and electrons into the channel from the anode and cathode, respectively. The gas is injected upstream and ionized by electrons that swirl azimuthally due to perpendicular electric and magnetic fields concentrated at the downstream end of the discharge channel. The ionized gas is then accelerated downstream by the electric field and neutralized by additional electrons emitted from the cathode. From ref. [9].

The main body of the thruster is made up of magnetic materials and coils to create a radial magnetic field across the channel. The axial electric field crossed with the radial magnetic field across the channel imposes an azimuthal drift on the electrons and they complete several rotations around the channel before being collected on the anode. During transit they collide with the neutral gas particles and ionize them. The ionized particles are then accelerated axially through the potential field within the channel and are largely unaffected by the magnetic field due to their relatively large mass. Downstream of the thruster the

ionized particle is then neutralized by an additional electron emitted from the cathode. As the particle is accelerated away from the channel the azimuthal electron current, known as the Hall current, attempts to shift but is held in place by the magnetic fields. Consequently this reactive force from the ejected particle is then coupled through the Hall current to the magnetic circuit, which is attached to the thruster body.

The plasma properties within the discharge channel of the thruster determine the overall operating characteristics and efficiencies—of particular interest are the azimuthally circulating electrons comprising the Hall current. The Hall current is located in the main ionization zone within the thruster channel and its characteristics can be determined from plasma properties. The azimuthal velocity of the electrons is due to the crossed field (ExB) configuration and can be determined as shown below

$$v_E = \frac{\boldsymbol{E}x\boldsymbol{B}}{B^2} \approx \frac{E_z}{B_r} = \frac{1}{B_r}\frac{d\phi}{dz} \quad , \qquad (1\text{-}3)$$

where ϕ is the axial electric potential within the plasma. The electric field in the radial direction and the magnetic field in the axial direction are generally small and can be neglected to simplify the equation. Multiplying the electron drift velocity by the electron number density, n_e, and the elementary charge of an electron, e, yields the Hall current density as

$$j_H = n_e\, e\, v_E \approx -n_e\, e \frac{1}{B_r}\frac{d\phi}{dz} \quad . \qquad (1\text{-}4)$$

The Hall current is the means of force transmission for an HET. The repulsive force between the accelerated ions and the circulating electrons is coupled to the thruster body through the magnetic field and the thrust generated by an HET can be calculated using

$$T = \int (\boldsymbol{j_H} \times \boldsymbol{B}) dA \approx |J_H| B_r \quad (1\text{-}5)$$

where T is the thrust and J_H is the Hall current. The main assumption of this equation is that the Hall current and radial magnetic field are constant in the channel. The use of probes to measure some of these properties provide insight into the distribution and behavior of the Hall current.

1.3 Hall Current Diagnostics

Several invasive [10], [11] and non-invasive [12]–[15] studies have characterized the Hall current distribution. Invasive options utilize probes to obtain plasma properties to calculate electron ExB drift velocities and thereby the current density distribution, as shown in Eq. (1-4). These methods perturb the thruster discharge plasma and may result in measurement errors. In addition, only steady state estimates of Hall current distributions can be made with this technique due to the long measurement time emissive probes and Langmuir probes require to obtain plasma properties throughout the entire channel.

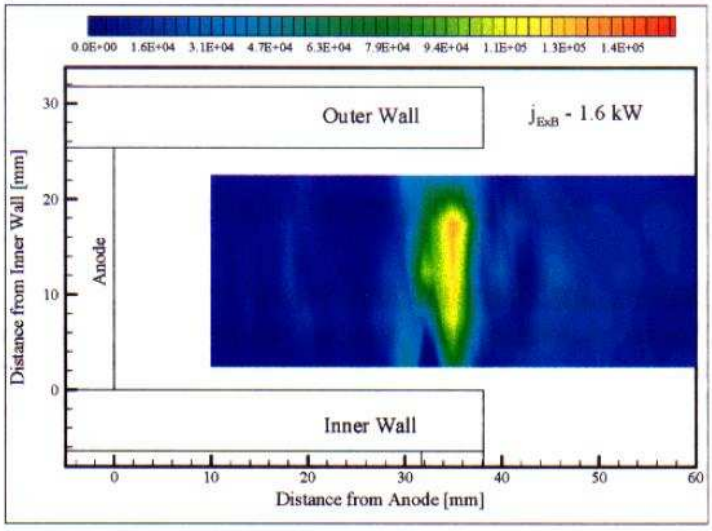

Figure 1.2: Hall current density measurement for a 1.6kW thruster acquired using invasive probe techniques. Units in A/m^2. From ref. [10].

Floating emissive probes can provide direct measurement of plasma potential without the need for a voltage sweep. This allows faster acquisition of the plasma potential within the channel, but there is still perturbation due to the physical presence of the probe [10], [16].

Several non-invasive diagnostics were developed in the late 1970s and early 1980s in Russia using pick-up coils wrapped around the channel [14], [15]. Since the non-invasive coil conception, other authors have attempted to reproduce and improve the process [12]. Up to the present time, all non-invasive experimental techniques utilized inductive coils surrounding the channel.

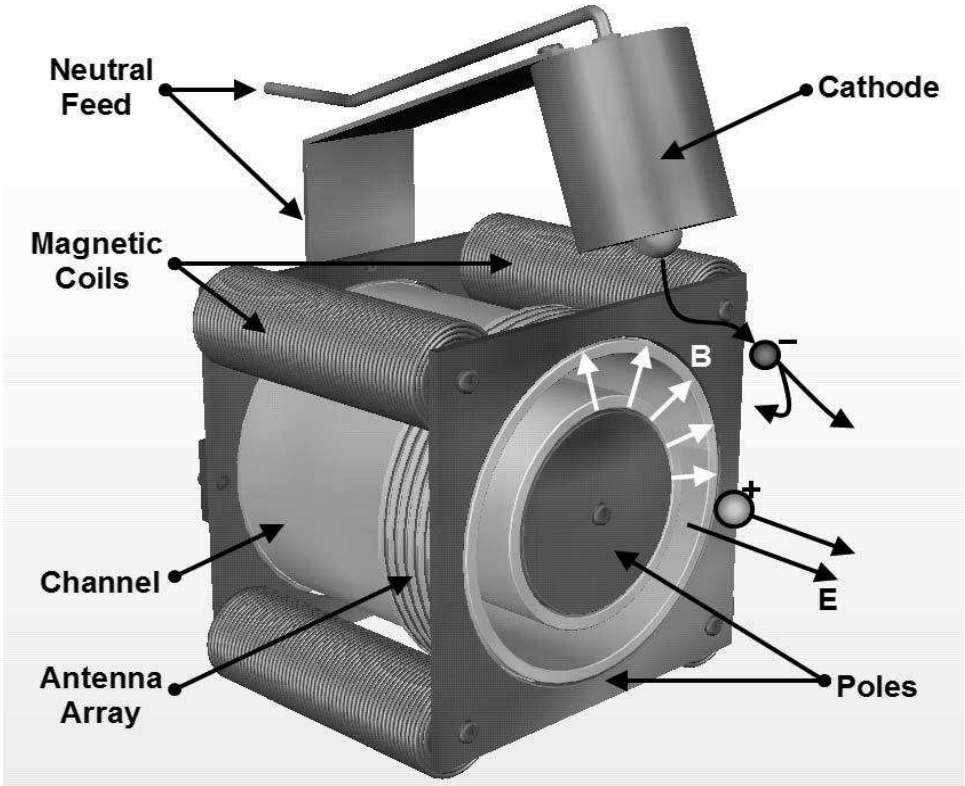

Figure 1.3: Diagram of Stanford Hall Thruster with non-invasive inductive coil array shown wrapping around the channel. Fig. 1 of [12]

The coils pick up the transient magnetic fields generated by the azimuthal current when the discharge current is suddenly switched off. This method requires a fast-switching power

supply to interrupt the thruster discharge current at a time scale of 100 ns. This method in principle could be used to measure nearly instantaneous Hall current structure, but in practice the measured data are still time-averaged and only steady-state data are reported.

This paper details an improved non-invasive technique that measures the induced magnetic field generated by the azimuthal current with an array of sensors and solves the inverse magneto-static problem to obtain the Hall current density distribution. This solution method has been previously developed and demonstrated numerically [17].

2. Development of Non-Invasive Hall Current Sensor

The measurement system presented in this thesis operates by sensing the change in the static magnetic field around the thruster when it is “on” and “off”. The magnitude of the change in the magnetic field can be on the order of 1 mG in certain regions not too far outside of the channel, and it is important to position the sensors properly to maximize the change in field the sensors measure due to the Hall current. This section will cover the design of the sensing array, starting with the direct and inverse magnetostatic problems and summarizing several design iterations.

2.1 Direct Magnetostatic Problem

The direct magnetostatic problem can be solved using an appropriate formulation of the Biot-Savart law. In free space the induced magnetic field, *B*, due to a known current, *I*, located at a known position in space yields the three dimensional magnetic field in the surrounding space.

$$\boldsymbol{B}(\boldsymbol{r}) = \frac{\mu_0}{4\pi}\int_C \frac{I d\boldsymbol{l} x \boldsymbol{r}'}{|\boldsymbol{r}'|^3} \tag{2-1}$$

The direct problem in an appropriate format is commonly used in finite element software to solve for the magnetic field. MagNet and the opensource FEMM software were used to simulate the CSU HET in the design of the thruster [18].

The magnetic field distribution within a Hall thruster is not completely axisymmetric in most designs. The thruster used for this research contains four outer coils equally spaced azimuthally around the thruster. A 3D model would be ideal, but was deemed unnecessary for this project. Instead a 2D model of the CSU HET was used to conduct placement studies for the sensors.

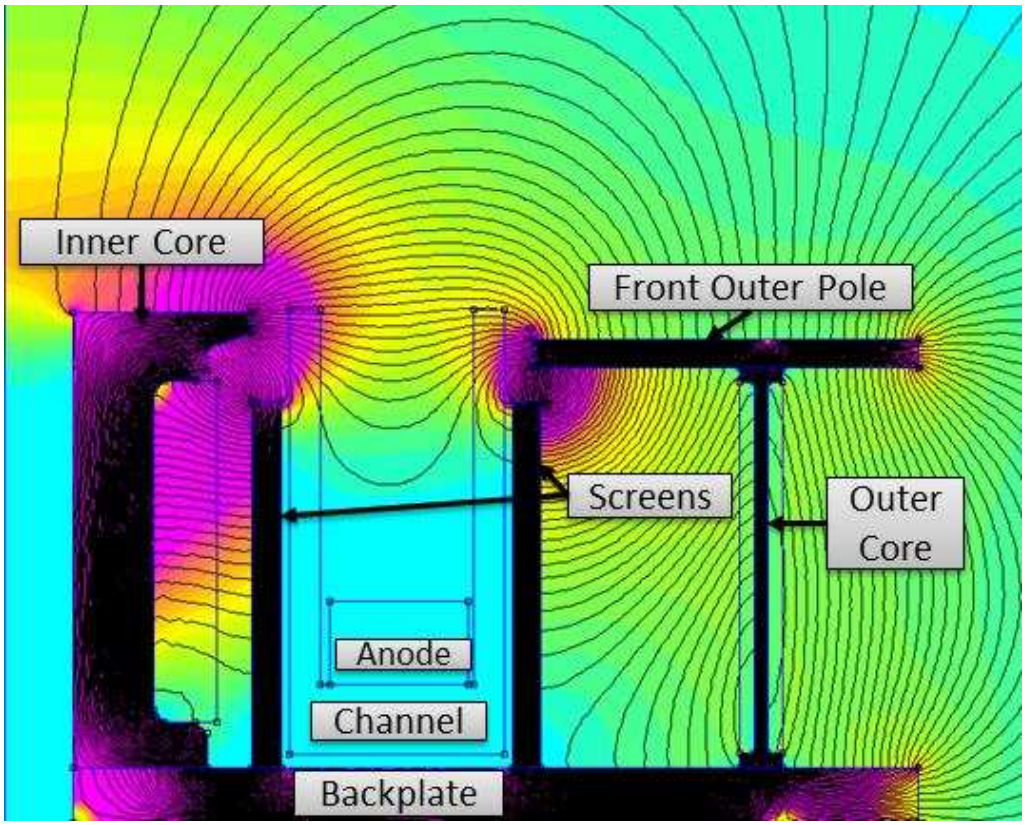

Figure 2.1: Cross section of simplified CSU 1.5kW HET in FEMM. Current is applied to coils to generate magnetic field distribution internal and external to the thruster.

In Figure 2.1 the outer coil is made to be significantly smaller in the model than in the actual design. This is because the 2D limitations of the simulation can be partially corrected by modeling the thruster to have a single outer coil that wraps around the entire thruster that is equivalent to the four outer coils on the real thruster. This magnetostatic model is what is manipulated to conduct field studies for sensor positioning. This program was chosen to be interfaced with MATLAB, thereby allowing many permutations to be run in a short amount of time. This model, while not completely accurate, provides an estimate for the design of the sensor layout.

2.2 Inverse Magnetostatic Problem

The inverse magnetostatic problem consists of solving for the current density using the surrounding measured magnetic field as input. This problem has been analyzed numerous times in previous work concerning integrated circuits [19] , bio-magnetics [20], [21], ferromagnetic material diagnostics [22] , thin shell ferromagnetic structures [23] , and plasma diagnostics [17].

The discretization and linearization of the direct magnetostatic problem leads to the matrix equation

$$AJ_H = B_m \tag{2-2}$$

where A is the Green's matrix relating the current density distribution to the surrounding magnetic field; J_H is the stacked column vector representing the two-dimensional azimuthal Hall current density distribution $j(r,z)$; and B_m is the measured and distributed magnetic field vector. For the inverse problem, the A matrix is know from calibration and the B_m vector is measured during testing. In this situation, the J_H vector is the unknown. The inverse problem can be formed in a linear least-squares format as

$$min\|AJ_H - B_m\|^2 \quad . \tag{2-3}$$

Typically the inverse solution to a magnetostatic problem is discontinuous and therefore ill-posed. This can cause small perturbations in the input data from the sensors propagate into large perturbations in the solution.[17] In addition, the problem is rank-deficient because the number of magnetic sensors, corresponding to the number of rows in A, are fewer than the number of current elements in the channel grid, corresponding to the number of rows in J_H.

Regularization of the problem uses a priori knowledge of the solution to apply a continuous smoothing function to the results. Since this problem resembles the Fredholm integral equations of the first kind, Tikhonov's regularization method was determined to be the best choice.[24] The general form for this problem can be written as

$$min\left\{\left||AJ_H - B_m|\right|^2 + \lambda^2\Omega(J)^2\right\} \tag{2-4}$$

where λ is the regularization parameter that controls the amount of smoothing applied to the solution by the regularization term $\Omega(J)^2$. The regularization term used to solve the Hall current distribution is known as the quadratic variation term and takes the form of

$$\Omega(J) = \left\|\frac{\partial^2 J_H}{\partial r^2}\right\|^2 + \left\|\frac{\partial^2 J_H}{\partial z}\right\|^2 + 2\left\|\frac{\partial^2 J_H}{\partial r \partial z}\right\|^2 \quad , \tag{2-5}$$

which has the effect of smoothing the second derivative of the solution to force a continuous distribution. We assumed all of the electrons circulate azimuthally around the channel in the same direction; therefore, a non-negativity constraint is also applied to the solution. Finally we also assume that the Hall current goes to zero at the channel walls, due to the dielectric walls, and far upstream and downstream of the maximum centerline magnetic field location. This condition is forced by an applied zero-current-density-boundary condition. The electron number density is equivalent to the ion number density and both are relatively low close to the anode where the axial electric field is also nearly zero. This causes the Hall current density to go towards zero. The electric field is also zero outside the channel downstream of the maximum magnetic field region, which forces the Hall current density towards zero. These physical bounds provide the inverse solver with additional constraints that improve the solution.

The solver function used within MATLAB requires an initial value of the current density to be given for the iterative conjugate gradient method used within the function. Several studies were run to verify that the initial guess did not affect the solution. Since it was shown that the initial guess was insignificant, an appropriately sized vector of zeros is passed to the function as the original values.

Determining the appropriate amount of regularization is critical to obtaining an accurate solution. The optimal regularization parameter is determined using the L-curve criterion.[25] A parametric plot of the discrete smoothing norm, also known as the regularization term $\Omega(J)$, versus the corresponding residual norm, $||A*J_H-B_m||$, for multiple regularization parameters is generated, and an example of typical data is shown in Figure 2.2. The "λ" resulting in the data point indicated in Figure 2.2 by the arrow is the best value to use for the regularization parameter.

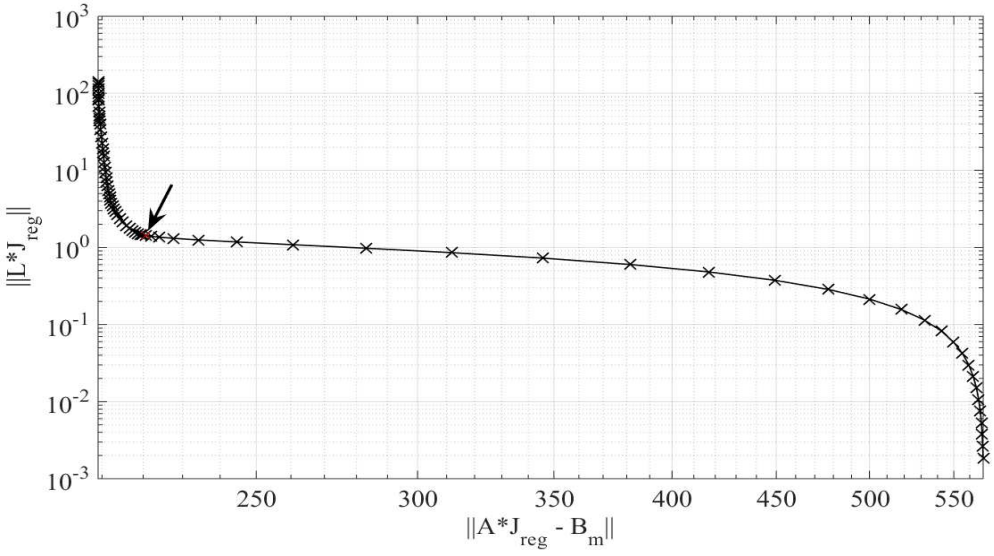

Figure 2.2: Example L-curve generated from an experimental data set. The arrow indicates the chosen regularization parameter for an optimal solution.

With both axes on a logarithmic scale, the curve forms a distinctive L-shape and the bend corresponds to the best compromise of smoothing and detail, characteristic of the minimization of two norms. Visual inspection or programmatic detection of the curve bend was used to yield the desired regularization parameter [17]. An ideal solution set would yield a curve with a sharp bend at the corner. A rounded edge is less desirable and is a result of the noise from the measurement of the magnetic field.

2.3 Magnetic Field Sensor

This application of magnetic field measurements pushes the operational limits of sensors available today. Many sensors are available and each has its own advantages and disadvantages. The overall desire was to have a device capable of detecting milliGauss changes in magnetic field intensity in a large background magnetic field with a response time of approximately 5MHz. A comprehensive study of the different options has previously been conducted [26], but ultimately the STJ-240 tunneling magneto-resistive (TMR) sensors made by Micromagnetics were chosen.

The sensors are a low-noise, low-power, high-sensitivity (~120mV/G) design. They are based on tunneling magnetoresitive (TMR) solid state technology, similar to what is used in giant magnetoresistive sensors (GMRs). The sensors consist of a tunnel barrier layer placed between two ferromagnetic layers. One of the magnetic layers is pinned such that it maintains its magnetization direction. The other magnetic layer is free to orient to the externally applied magnetic field. The orientation of the free layer relative to the pinned layer changes the effective resistance of the sensor and the resistance can be measured to obtain field intensity. All of the sensor specifications regarding general sensitivity, operative voltage, noise characteristics, and more can be found in the specification sheet [27].

2.4 Sensor Positioning

The nature of the inverse solution forces one to minimize the amount of noise injected during data acquisition. The maximization of the signal-to-noise ratio and the change in the magnetic field due to the Hall current have a significant effect on the solution. Simulations of the CSU HET were created to generate differential magnetic field plots to assist in placement of the sensors. The same 2D FEMM model shown in Figure 2.1 was used as a baseline for the model. A Hall current was placed in the channel just upstream of the maximum centerline radial magnetic field location as shown in Figure 2.3.

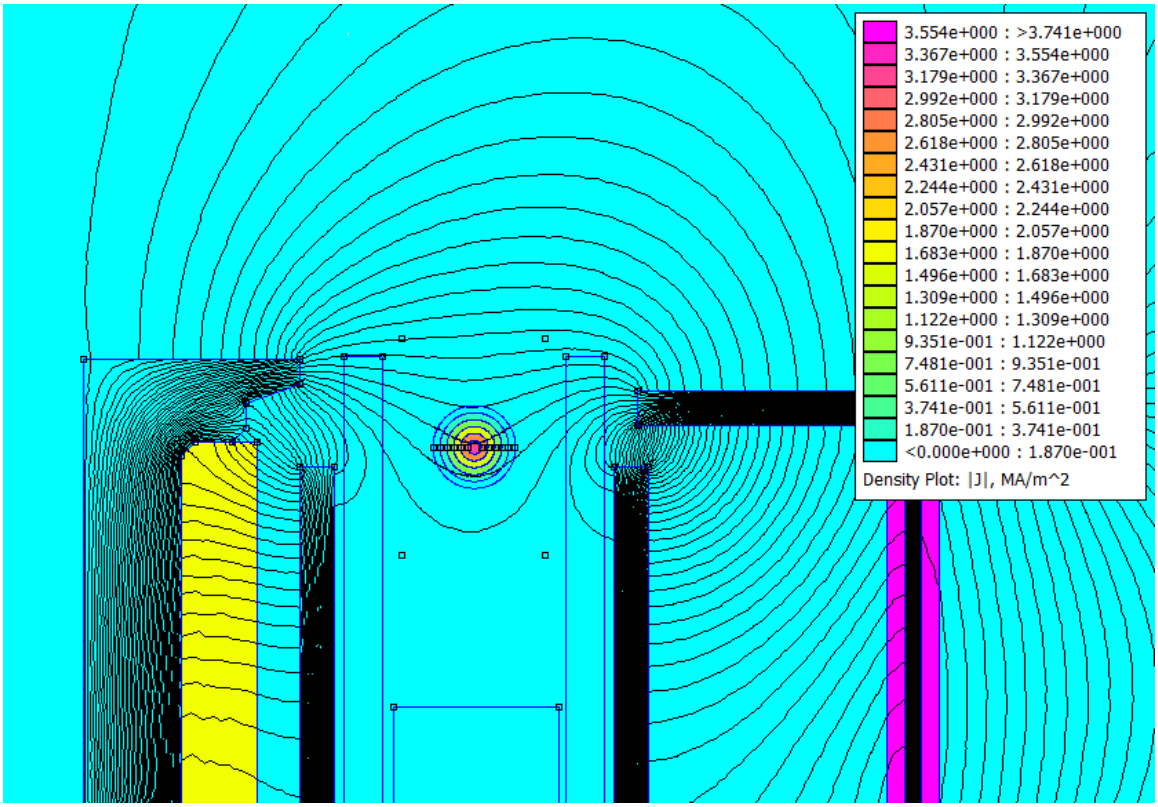

Figure 2.3: FEMM Hall current simulation model. Magnetic field lines and current density are shown.

The Hall current was only meant to provide an approximation and not intended to be a high fidelity simulation. The simulation was run without the Hall current present to

establish a background measurement. Then the current for each of the circular zones was determined appropriately to create a Gaussian distribution of the Hall current density. Once a field map had been created for both states, the data from the area of interest were calculated and a differential map was created.

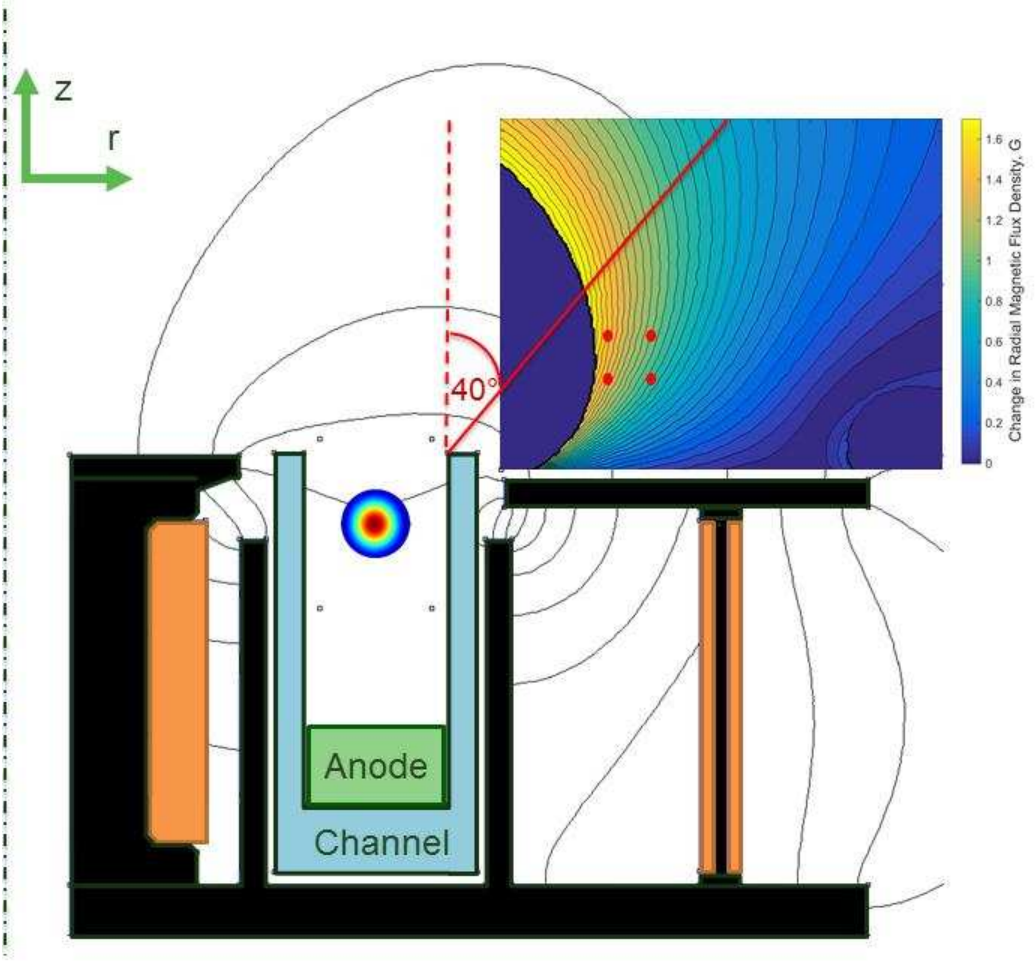

Figure 2.4: Difference in radial magnetic field (B_r) due to the Hall current. Red line represents placement bound for sensors such that they are not in the plume. The four red dots are locations where sensors could be located.

The domain downstream of the front outer pole piece was chosen due to its proximity to the Hall current while not invading the structure or the plume of the thruster. The dark area on the left side of the plot represents the locations where the static field is above 30 G, which is too high for the sensors to operate in. Strategic placement of the sensors is

accomplished by putting them in a region of high field differential while remaining in their operating range and outside of the plume, and example locations that are suitable are represented by the four red dots in Figure 2.4. A previous study of the problem determined seven to 10 sensors were ideal to obtain suitably resolved solutions of Hall current density [17]. Due to limitations of the data acquisition device available for this thesis, eight sensor placements were chosen with four measuring the axial field and four measuring the radial field. Figure 2.5 shows arrow in the eight locations that were chosen.

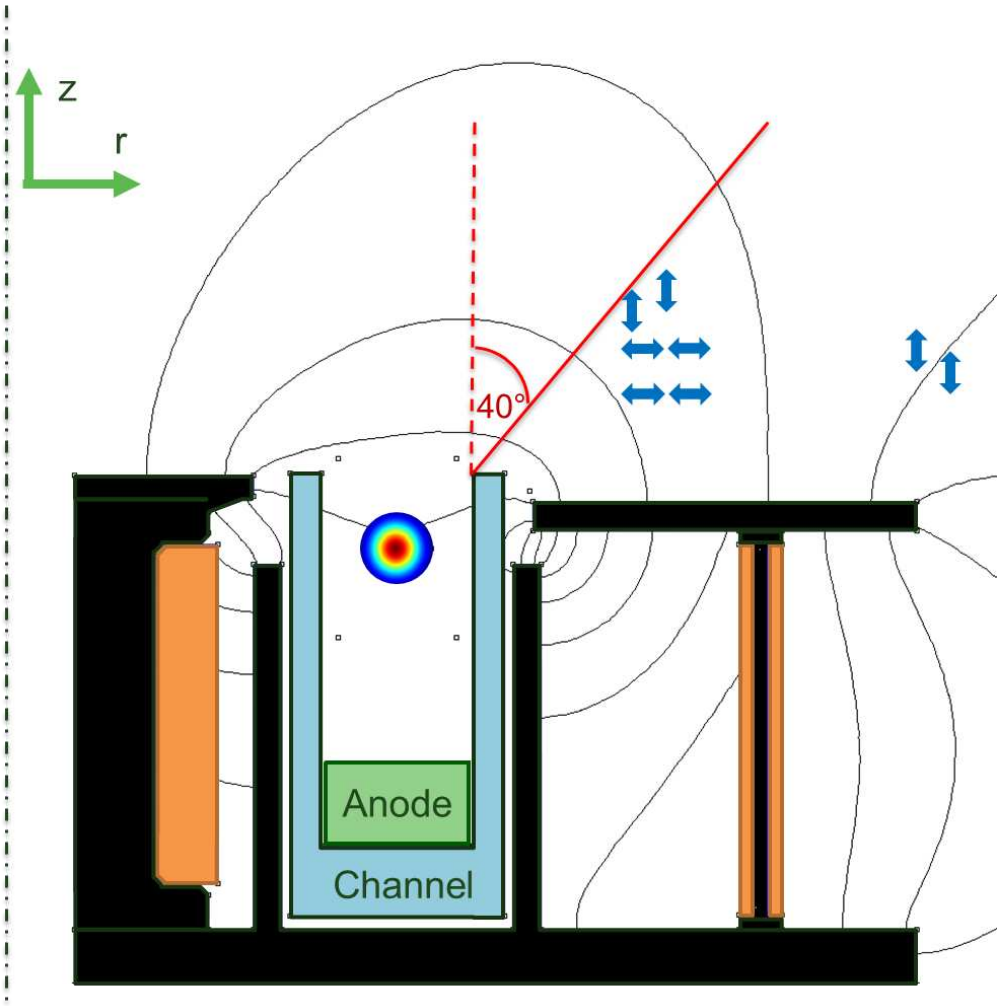

Figure 2.5: Chosen sensor positions based on differential simulations. Blue arrow indicate direction of measurement.

Studies were conducted to look at placing the axial sensors in other areas around the thruster. The locations shown in Figure 2.5 were determined to be optimal for seeing the largest field change due to the Hall current while staying out of the plume and out of high magnetic field intensity regions. The radial sensors were in an equally spaced four quadrant grid close to the downstream face of the outer pole piece. The majority of the magnetic flux coming out of the iron in this location was in the axial direction, allowing the radial sensors to be placed closer to the thruster. Further improvements could be made by conducting an internal placement study for integrating the sensors into the HET.

2.5 Two Axis Probe Sensor Design

The first iteration of the experiments utilized a probe configuration of the sensor. The ability to vary the positioning of the sensors would assist in verifying the locations determined by the simulations. The probe would be attached to a motion stage downstream of the thruster. The sensors have a unidirectional sensing area of 1 sq. μm. The sensors can operate in a maximum field of 30G and temperatures up to 150°C before failure. The TMR sensors experience variations in sensitivity due to thermal effects but it was determined that no active cooling system would be used for this design since the probe could be moved away from the thruster in the case where the sensors began to overheat.

The MTJ sensor sits on a custom designed circuit board with dimensions of 0.5 in. x 1.7 in. x 0.063 in. (W x L x H). The board fits along the center axis of a 5/8 in. outer diameter stainless steel tube that is attached to a cast aluminum box using a Swagelok tube bulkhead connector. Three Triax cables are used to link the board's measurement and power signals to the isolated Triax connectors on the aluminum housing, as shown in Figure 2.6. A 22 gauge wire is used to connect the ground plane of the circuit to the outer housing. The outer

housing is then grounded to the chamber through the mounting fixture on the motion stage. The entire sensor housing was wrapped in Kapton tape to reduce sputtering.

Figure 2.6: Two Axis Sensor Probe housing layout and design.

The sensors were operated in a voltage divider configuration where the voltage measurement is made across the passive resistor. As the resistance of the TMR sensor changes the voltage drop across the measurement resistor changes respectively. A National Instruments (NI) USB-6366 data acquisition board (DAQ) was used to sample both sensors at 1MHz, simultaneously. A 3.7V Li-Ion battery powers the circuit. A battery supply was chosen to eliminate any ripple effects that could be caused by a DC power supply. The two layer circuit board contains two TMR sensors placed at the same location on the circuit plane, but on opposite layers rotated 90° with respect to each other, as shown in Figure 2.7. One of the sensors detects the radial field while the other measures the axial field.

The following two figures show the full layout of the top and bottom layers of the board. Figure 2.8 is the horizontally flipped image of Figure 2.9. Both of the layers share the same power connection through the P+ and P- bias. Pads C1 & C3 and C2 & C4 are for 1.0 μF and 0.1 μF capacitors, for each respective circuit, which assist in eliminating voltage fluctuations picked up in the power transmission cable. The GND via is used to connect the grounding plane of the circuit to the outer casing. The RS and RS1 pads are both 1200 Ω resistors and make up the lower part of the voltage divider circuits. The M+ and M- pads are were the measurement cables are soldered to transfer the voltage differential signal to the NI DAQ. The RB and SH pads were added in the event that the shield of the Triax cable was used to balance the circuit relative to the DAQ [28]. Currently, these pads are not in use since the noise levels are within an acceptable range and less than the DAQ absolute accuracy of 440 μV, determined using the specification sheet for the NI USB 6366. The measurement pads are spaced equidistant from the RS resistor to create a similar path of travel, and therefore similar noise pickup, for both measurement leads. For a differential measurement this helps to ensure the maximum effectiveness of the common mode rejection (CMR) of the differential amplifier.

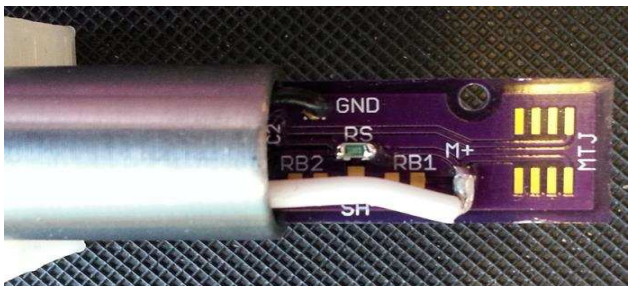

Figure 2.7: Two sensor probe tip. Double sided circuit board that measures the axial and radial magnetic fields.

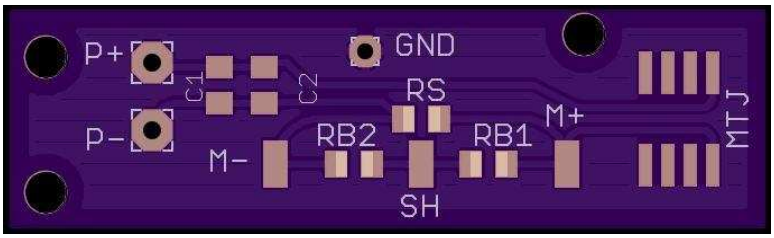

Figure 2.8: Radial field sensing circuit. Circuit layout for two axis probe design.

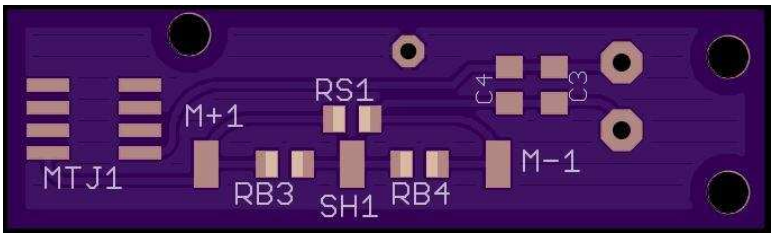

Figure 2.9: Axial field sensing circuit. Board layout for two axis probe design.

A schematic of the circuit layout is shown in Figure 2.10 including the DAQ, vacuum chamber wall, and internal and external circuit components. Hermitically sealed Triax feedthroughs were used to pass all of the signals through the chamber.

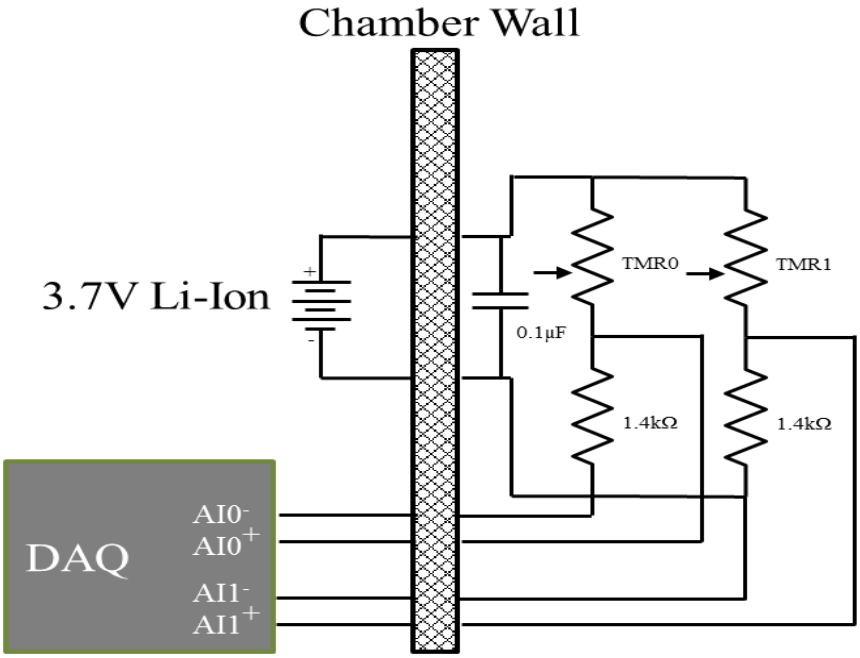

Figure 2.10: Circuit diagram for two axis probe sensor.

2.6 Eight Sensor Array Design

The two axis probe design was meant to be a prototype leading up to the final design phase. The second iteration of the sensor utilized all eight channels available in the DAQ, which were simultaneously sampled at 2 MHz. Using eight sensors provided more diverse information about the induced field to allow for improved resolution and convergence of the inverse solution. In addition, the simultaneous acquisition of the sensors yielded temporal solutions to be constructed. Placement of a magnetic sensor array near the exit plane of the thruster, as shown in Figure 2.11, allowed for stationary measurement of the induced field.

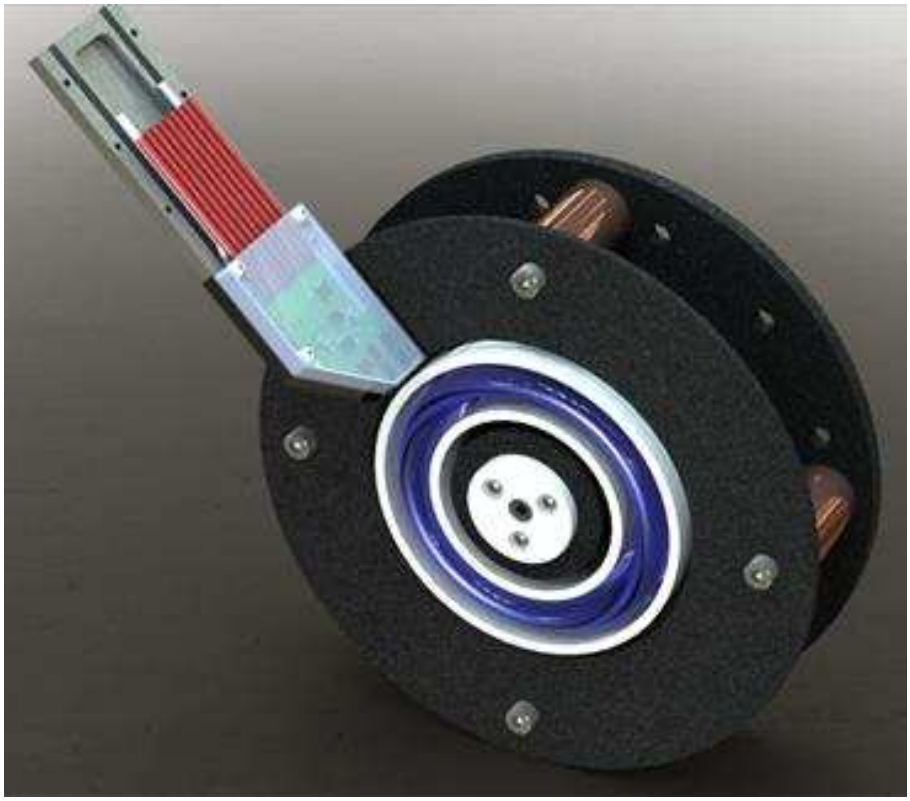

Figure 2.11: Magnetic sensor array rendering. Shows the design and positioning of the sensors relative to the CSU 1.5 kW HET.

The harsh environment near the thruster limits sensor placement. Simulations of the magnetic fields, with and without a simulated Hall current, downstream of the front outer

pole piece of the thruster were shown above. The arrangement of the sensors on the board in the rendering match that of Figure 2.5. The axial sensors were placed along a curve downstream on the printed circuit board running from the inner wall of the board to the outer wall. The sensor array circuit shared a single power bus between all of the sensors. The TMR sensors are ESD sensitive and voltage sensitive, therefore we chose a fixed voltage/voltage divider measurement scheme because the current flowing through the sensor does not need to be regulated.

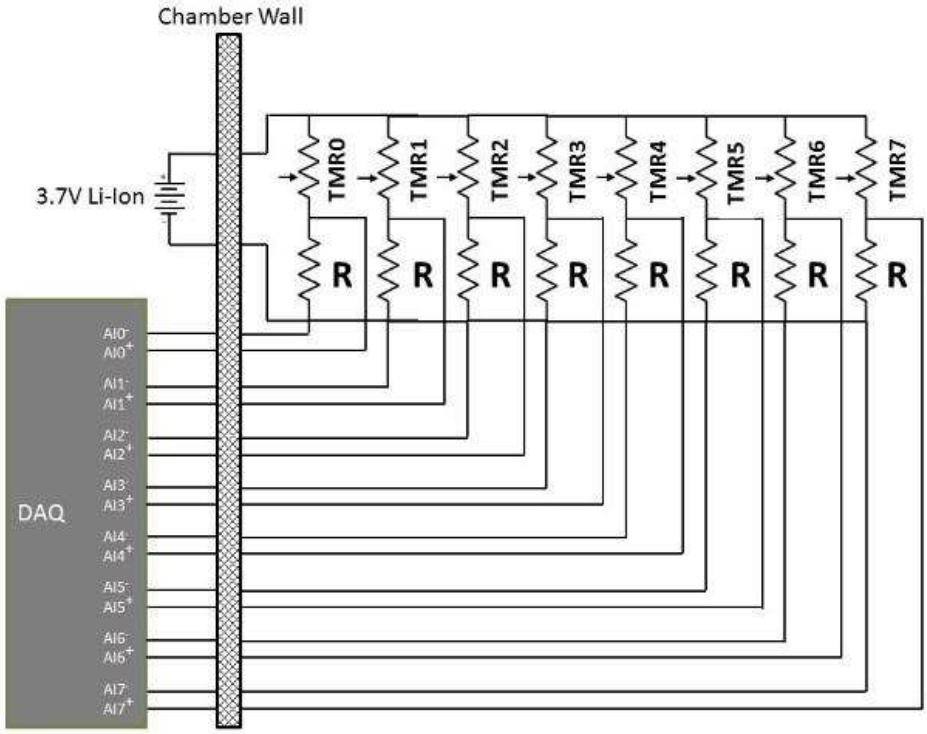

Figure 2.12: Eight sensor magnetic circuit schematic. All eight sensors are wired in parallel in a voltage divider configuration where R = 1.4 kΩ. The battery and DAQ are outside vacuum.

The resistor values in the schematic were chosen to create an approximate 1:2 resistance ratio to maximize the voltage drop across the passive resistor. This has the benefit of increasing the signal-to-noise ratio without exceeding the 2V full scale range of the DAQ.

The casing design consists of three main components: the board, the outer casing, and the mounting plate. The outer casing is machined out of stainless steel and contains several mounting points for the board and the mounting plate. Two graphite covers fit over the top and bottom of the outer casing to shield the sensor from plasma. The mounting plate is also made of stainless steel and has a U-shaped slot machined along it to hold a 1/8 in. stainless steel tube for active water cooling. The tubing is secured using silver filed epoxy to ensure sufficient thermal conductance. The outer casing is then secured to the mounting plate with four screws with a silver conductive vacuum paste between the two parts. A thermocouple is attached to the circuit board underneath one of the board mounting screws. This allows for monitoring of the board temperature to make sure it does not exceed 80 degrees Celsius.

3. Experimental Setup and Analysis

The CSU 1.5 kW Hall thruster was used for the testing and verification of the Hall current sensor system. Several tests were performed at different operating power level, magnetic field, and cathode configurations. This chapter will cover the facilities and equipment used for this testing. Information regarding the calibration and analysis of the acquired data is also presented.

3.1 Vacuum Testing Facility

The CEPPE lab has several vacuum chambers used for testing. For this research, the testing is conducted in the 1.7 m diameter by 4.6 m long chamber. The chamber is pumped by a Leybold DryVac 650 roughing pump, two Varian HS20 diffusion pumps, and two cryosails. The chamber has a maximum pumping speed of 38,000 L/s for Krypton with a base pressure of 1.4e-6 Torr after four hours. The pumping speed without the cryosails is 19,000 L/s. The pressure during Krypton operation is 4.8e-5 Torr at 70 sccm (without the cryosails), a common mass flow rate used for testing the 1.5 kW HET. High-purity (99.999% pure) xenon and krypton propellant is supplied to the HET from compressed gas bottles through stainless steel feedlines. Brooks 5850E mass flow controllers meter the anode and cathode propellant flow. The mass flow controllers have an accuracy of ±1% full scale. The ion gauge, Granville Phillips S260 with an accuracy of ±25%, is mounted to the door of the chamber and sits upstream of the thruster. There is a graphite beam dump, located 2.8 m downstream of the thruster, which protects the cryosails from the thruster plume.

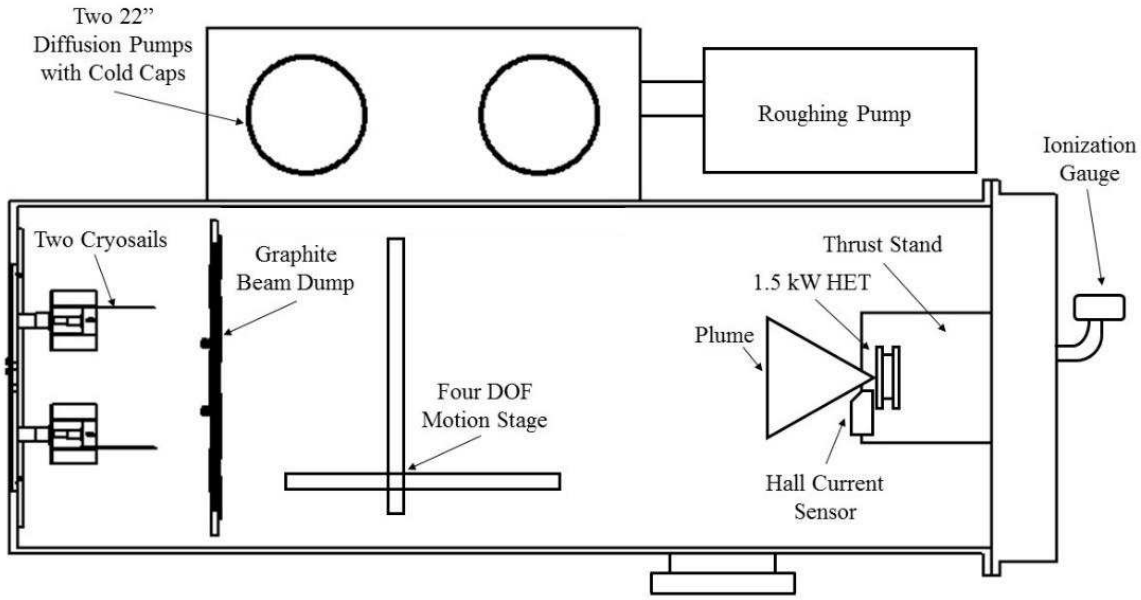

Figure 3.1: Schematic diagram of vacuum chamber test facility. Detailed cross-section view above the chamber.

The discharge current and voltage is supplied by a Sorenson 3kW DC power supply across two parallel 54μF oil filled capacitors and in series with a 1.4Ω 110W resistor to stabilize the output. During testing the discharge current and oscillations, and cathode to ground voltage are recorded. The discharge voltage, magnetic coil voltage and current, mass flow rate, and keeper to cathode voltage are recorded manually. The discharge current is monitored using a TAMURA L07P010S05 Hall effect sensor capable of measuring currents up to 10A with a 5 μs response time. The output of the Hall sensor is read by a Quant Asylum QA100 oscilloscope at 2.5MHz and post processing scripts are used to yield the primary discharge current oscillation frequency. The average discharge current is measured by sensing the voltage drop across a 5mΩ shunt placed on the cathode power line. The cathode-to-ground voltage and shunt voltage are both recorded every second by an Agilent 34970A. Operational photos of the thruster were taken using a Nikon D600 camera with a Nikon 24-140mm lens set to f11 with manual focus.

3.2 Thrust Stand

All thrust measurements are performed using a hanging double pendulum thrust stand. Prior to testing, the thruster is operated for two hours to allow for outgassing of all the components and for thermal stabilization of the thrust stand. Many facilities use inverted-pendulum thrust stand designs for greater operational range and sensitivity [30], [31]. They also have a high dependence on thermal stability of the flexures to maintain accuracy, which is usually mitigated through the use of a cooling shroud [32]. The simplicity, stability, and low cost of a hanging pendulum thrust stand are the main factors in choosing this design for our tests. Thermal variations can cause drift and sensitivity changes so repeat calibrations are used when the system reaches thermal equilibrium to mitigate these sources of error. The thrust stand is in a double hanging configuration to increase the stability of the system and eliminate the effects of thruster placement [33]–[35].

The main thrust stand structure consists of an extruded aluminum frame mounted to the door of the vacuum chamber. Four stainless steel bands hang from the top of the frame and attach to the free moving graphite plate near the bottom of the frame. Three gas feed lines using 1/16 in. tubing are formed into an accordion style fold pattern to minimize bias. Likewise, all of the power cables are draped in a waterfall configuration between the door and the mounting plate to minimize their influence. Multiple single cables, made of 19 strands of 34 gauge silver-coated copper wire with Teflon insulation, are used for all the electrical connections on the thruster. Calibration during thruster operation accounts for the influence of the gas line and wire stiffness. The motion of the thrust stand is measured by an LVDT placed near the top of the frame with the core attached to a graphite rod connected to the bottom plate. The LVDT is excited and filtered by a SR810 lock-in amplifier that has an

output noise level below the absolute resolution of the National Instruments (NI) NI-PCI6036E data acquisition card used to measure the SR810 signal. The DAQ card has 16 bit resolution and samples the lock-in signal at 10 kHz and averages 1000 samples to achieve a 10 Hz update rate. The raw signal from the lock-in amplifier, as measured by the DAQ, is used to determine the resolution of the thrust stand. The standard deviation of the averaged signal provides a confidence band for the measured voltage value. This error is then propagated through the calibration curve to obtain the resolution. The thrust stand has a maximum resolution of ±0.5 mN and the real time interpolation error is constantly updated and displayed with a greatest value that is always less than 4% of the thrust. As mentioned above, the long-term thermal drift is corrected by calibrating several times during testing as well as prior to and after the thruster is operated. The drift offset is obtained by shutting off the thruster, which is then applied to correct the thrust measurement. We have used ref. [36] to guide all of our thrust stand uncertainty analysis.

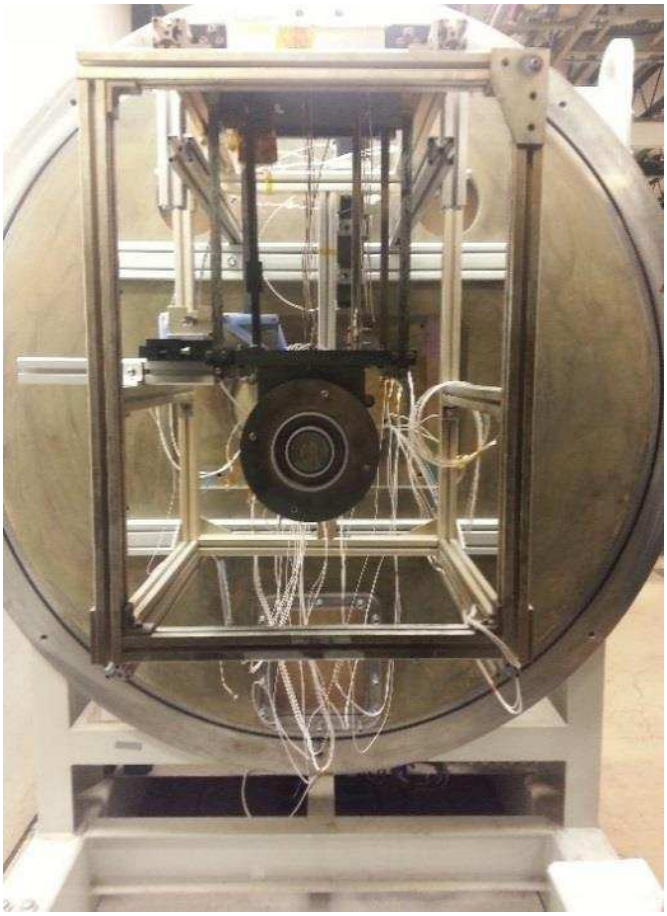

Figure 3.2: CSU hanging pendulum thrust stand used for all thruster testing with a 1mN accuracy.

The calibration system for the thrust stand consists of a silk string suspended between the free-hanging plate and the chamber wall. Up to five weights are added at the

center of the string to create a tension force on the thrust stand. The application of the weights create known calibration forces with a maximum of 63 mN. All thrust measurements outside of this range are extrapolated and the appropriate extrapolation error is calculated [36]. The linearity of the system allows extrapolation of the thrust values while maintaining a standard error below that reported above. The error from extrapolating outside the calibration values is negligible in comparison to the other sources of error. One source of predicted error in this calibration method is the change in the string angle relative to the vertical as the distance between the plate and the chamber wall decreases. An analysis of this situation shows the angle in the string only changes by 0.1% and this effect on error is mitigated by solving a non-linear equation for the string angle at each calibration data point. The advantages of our taut string technique is that no pulley is required. The lack of a pulley removes any friction or pulley roll off error from the calibration.

3.3 CSU 1.5kW Thruster

The CSU 1.5kW HET is an SPT style thruster with a ceramic borosil ($BN\text{-}SiO_2$) channel that is shown in Figure 3.3 to Figure 3.5. Design details and operating characteristics have been previously reported by Martinez et al [18]. The following is a summary of the information contained within.

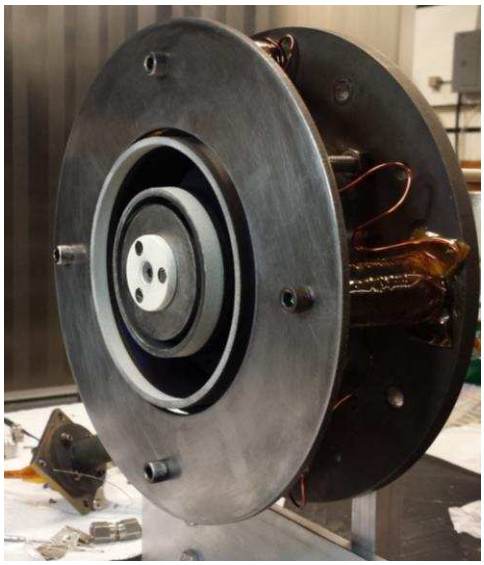

Figure 3.3: CSU 1.5kW HET based on SPT style design.

The channel dimensions are 104 mm O.D. with a width of 17 mm and a length of 32 mm. Four outer coils wired in series and separated by 90° coupled with a center coil generate the channel magnetic field, which features a plasma lens topography, as

shown in Figure 3.6. MagNet was used to design the field topography and ensure the magnetic materials used in the thruster were not saturating. The radial magnetic field along the centerline of the channel peaks just downstream of the exit plane and reaches a minimum value of ~3% of the maximum centerline magnitude at the anode. Minimizing the field near the anode decreases the anode sheath fall voltage and helps maintain current continuity.

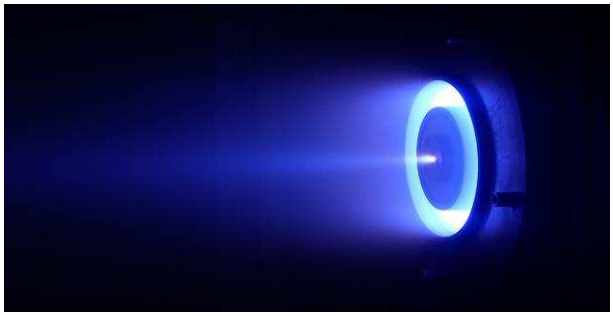

Figure 3.4: CSU HET operation at 1.5 kW on Krypton at 4.0 mg/s and a discharge voltage of 300 V with a center mounted electride cathode.

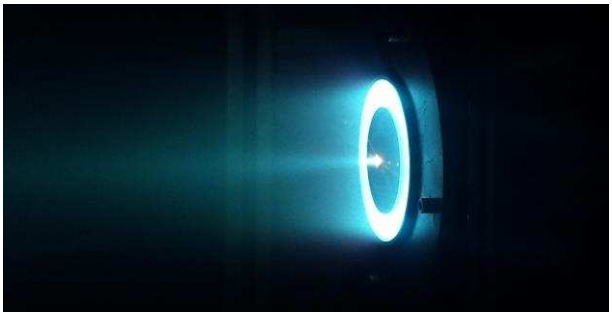

Figure 3.5: CSU HET operation at 1.5 kW on Xenon at 5.5 mg/s and a discharge voltage of 300 V with a center mounted electride cathode.

A center-mounted heaterless electride hollow cathode provides electron emission and minimizes plume divergence. An additional external tungsten impregnated barium oxide 6.4 mm diameter cathode was used during testing as well for comparison. The thruster is capable of operating at power levels ranging from 0.5 kW – 2.5 kW with both krypton and xenon. The nominal operating point of 1.5 kW and 300 V was used for the majority of testing and experimentation with additional testing at 1.0kW and 2.0kW power levels using Krypton.

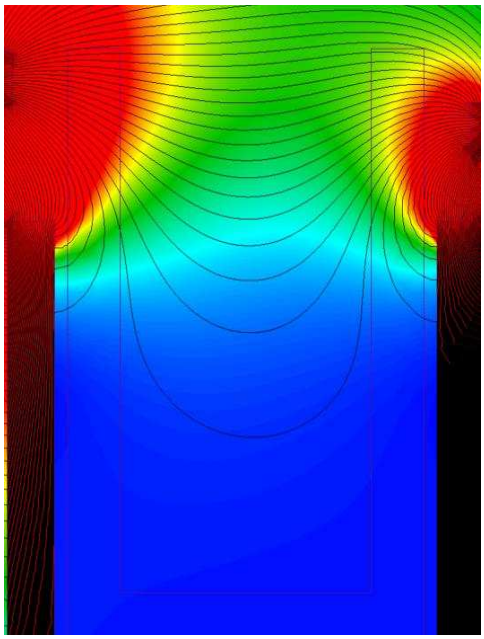

Figure 3.6: CSU HET magnetic field topology.

3.4 Hall Current Density Sensor

A crucial step in operating the sensor involves calibrating the setup to obtain the Green's matrix for the inverse solver. The inverse regularization solution method requires that the Green's matrix, A, be known. This is only achievable with our laboratory thruster by calibration. The Green's matrix is specific to each configuration of the thruster and sensor. The calibration sets the spatial and magnitude relation between the measured magnetic field and the distribution of the current. Therefore, if the sensor location is changed, the thruster magnetic circuit is modified, or the surrounding environment is altered; then a calibration must be redone. It is possible to achieve a calibration through a simulation [17], but this was not attempted in our study. Although not attempted, we describe how to construct a Green's matrix below using simulations because this is illustrative of how one experimentally accomplishes the same task.

3.4.1. Simulated Calibration

Simulating the calibration routine is possible and desirable if a high fidelity model of the thruster and the environment can be created, allowing one to calculate the Green's matrix computationally. The difficulty with this process is accounting for all the variables in the system. The B-H curves of the magnetic materials used to construct the thruster can vary from the simulated materials and as a function of temperature. Also, a full three-dimensional magnetostatic model of the thruster is necessary and can be computationally intensive to obtain.

A simplified magnetostatic model was created to demonstrate how the inverse solution algorithm made to work. The open source magnetostatic software, FEMM, was used to model the 1.5 kW thruster in two dimensions. A radial cross-section of the thruster, shown

in Figure 3.7, along with an array of copper wires in the channel are used to simulate point sources of current representative of a discretized Hall current.

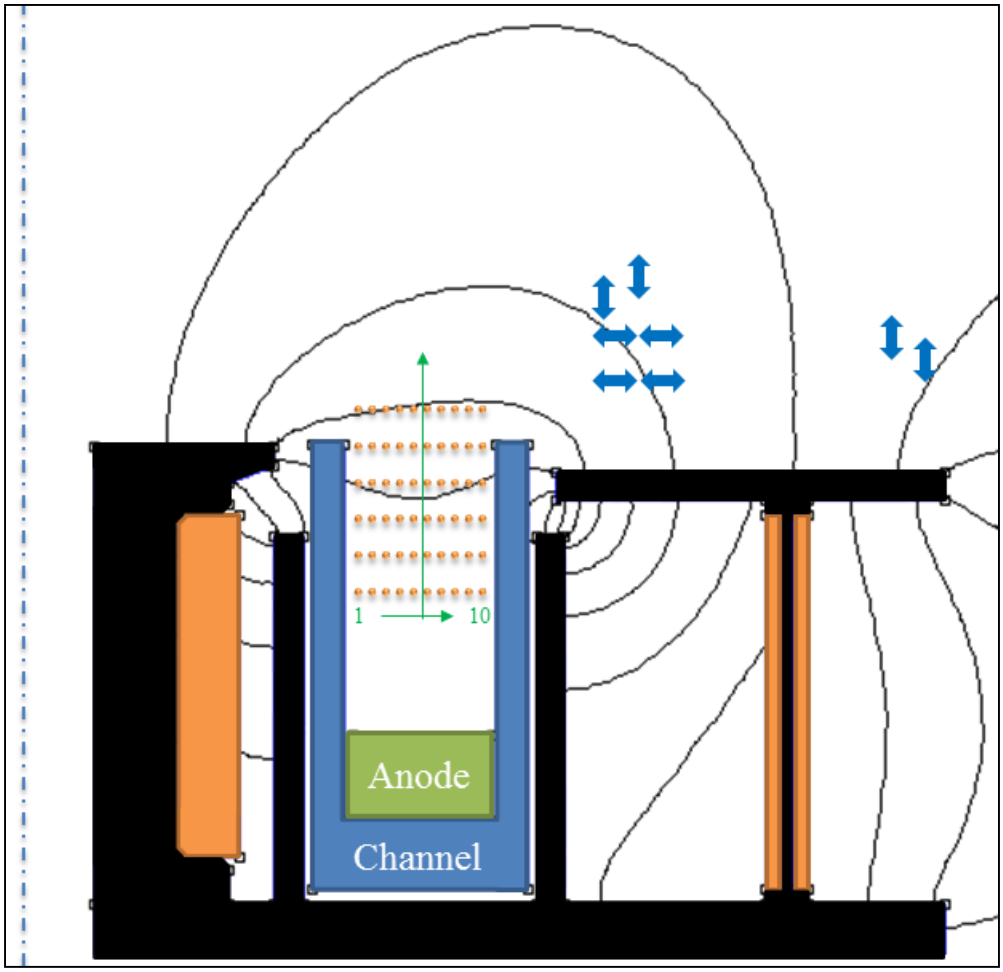

Figure 3.7: FEMM calibration simulation. The 10 copper wires are shown in the channel and numbered 1 through 10. The wires are moved further downstream as the calibration progresses. The arrows represent the sensor positions and sensing direction.

Ten 22 gauge copper wires are equally spaced in the radial direction on the same axial plane within the thruster channel. The axial and radial magnetic field values are recorded at the intended sensor positions, one through eight, downstream of the front outer pole face in the positions shown in Figure 2.5. This provided the background field due to the thruster, shown as $B_{background}$ in Eq. (3-1). Next, a known current was applied to each copper wire individually. The magnetic field values were queried at the sensor positions once again,

represented as B_{wire} in Eq. (3-1). The difference between these two measurements, B_{Δ}, provides the desired value. In Eq. (3-1) r is the radial position, z is the axial position, and S is the sensor that is making the measurement.

$$B_{\Delta}(r,z,S) = B_{wire}(r,z,S) - B_{background}(r,z,S) \tag{3-1}$$

The wires were then moved to a different axial plane and the process was repeated to create a calibration grid within the channel. It is known that the Hall current resides near the maximum radial magnetic field and the calibration grid domain was determined based on the predicted location of the Hall current [10], [37]. The Green's matrix was constructed once the induced magnetic field was known at the sensor locations due to a known current in each wire. Results of the calibration yield a two-dimensional array for each sensor containing the induced magnetic field for all of the wire coordinate locations, shown in Eq. (3-2).

$$\begin{bmatrix} B_{\Delta}(r_1,z_6,S_1) & \cdots & B_{\Delta}(r_{10},z_6,S_1) \\ \vdots & \ddots & \vdots \\ B_{\Delta}(r_1,z_1,S_1) & \cdots & B_{\Delta}(r_{10},z_1,S_1) \end{bmatrix} \tag{3-2}$$

Each sensor has a corresponding two-dimensional calibration matrix organized and flattened into a column vector. All of the vectors are then stacked row wise to form the Green's matrix, as laid out below.

$$\begin{bmatrix} B_{\Delta}(r_1,z_6,S_1)\cdots B_{\Delta}(r_{10},z_6,S_1) & B_{\Delta}(r_1,z_5,S_1)\cdots B_{\Delta}(r_{10},z_5,S_1)\cdots & B_{\Delta}(r_1,z_1,S_1)\cdots B_{\Delta}(r_{10},z_1,S_1) \\ & \vdots & \\ B_{\Delta}(r_1,z_6,S_8)\cdots B_{\Delta}(r_{10},z_6,S_8) & B_{\Delta}(r_1,z_5,S_8)\cdots B_{\Delta}(r_{10},z_5,S_8)\cdots & B_{\Delta}(r_1,z_1,S_8)\cdots B_{\Delta}(r_{10},z_1,S_8) \end{bmatrix}$$

The number of rows correspond to the number of sensors used, two for the two axis probe and eight for the stationary array as shown in the matrix above, and the number of columns is equivalent to the number of radial wire locations multiplied by the number of axial wire

locations. In the case of the setup shown in Figure 3.7, the model included 60 columns and eight rows in the Green's matrix, represented by the matrix above.

3.4.2. Experimental Calibration

Due to limitations in the accuracy of the magnetostatic simulation of our thruster, calibration is accomplished experimentally. The calibration method is what determines the size of the solution domain. A general layout of the calibration setup is shown below in Figure 3.8 where the thruster is firing to the right.

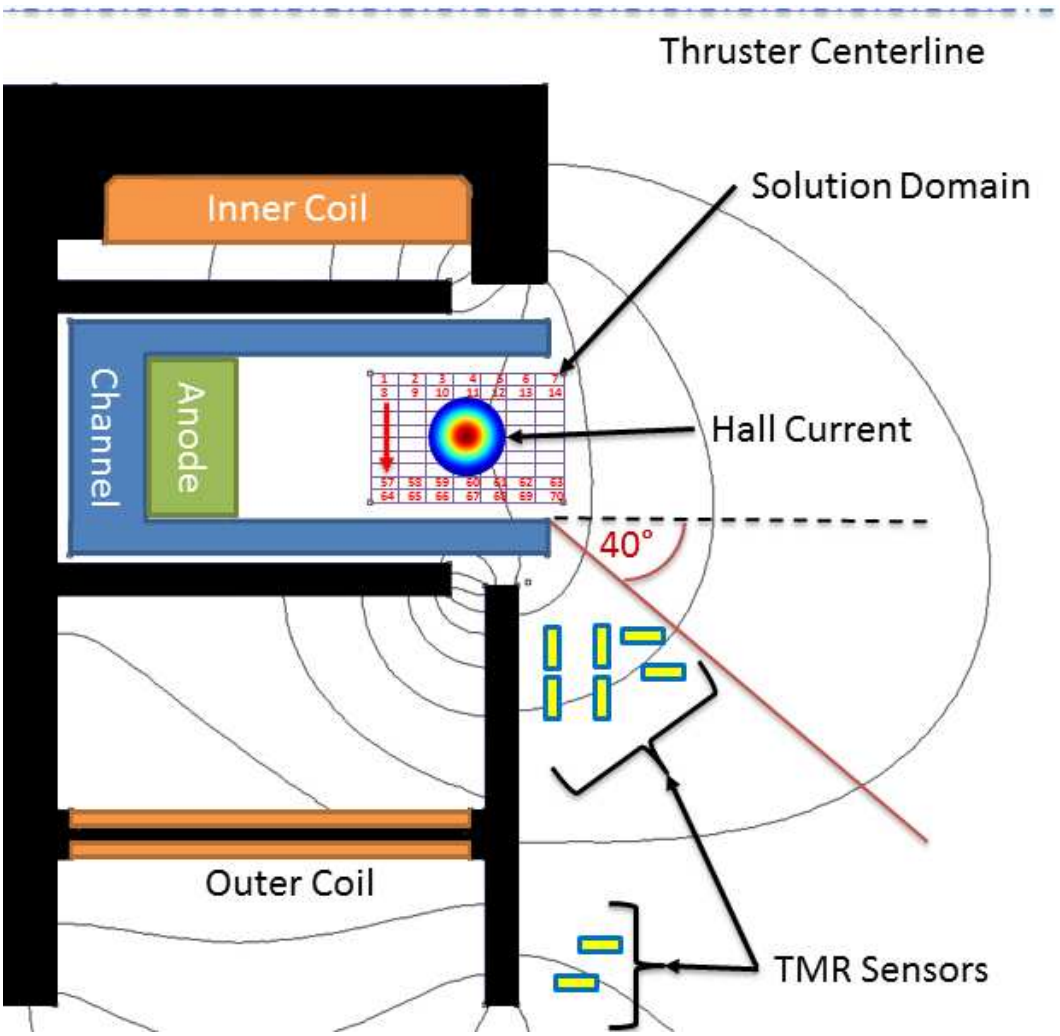

Figure 3.8: Cross-section of CSU HET calibration setup. The numbered grid represents all of the calibration locations within the channel. With a single wire moved to each location, the sensors measure the induced magnetic field relative to the thruster background field. The

more discretized the grid is, the more resolution there is in the Hall current solution for a given number of sensors.

An azimuthally-circulating current within the channel needed to be input in multiple locations to achieve calibration. Initial designs consisted of a single wire ring that was moved to all of the desired grid locations as illustrated in Figure 3.8. This process was deemed too tedious and thus an improved design was implemented that contained wires for all of the desired radial positions within the calibration tool.

A holder with ten 22 gauge copper magnet wires was designed to fit inside the ceramic channel of the HET, shown in Figure 3.9**.** The main body is made of 3D-printed ABS plastic with super glue used to hold the wires within the channel. A polycarbonate tube bundles all of the 20 leads leaving the coil. All of the leads on one end of the coil circuit are joined by a single connector. The other end of the circuit is divided into ten labeled connectors to allow for individual charging of each wire. All of the copper magnet wires are approximately equally spaced radially on the same axial plane. The first radial position shown as *r1* in Eq. (3-2) corresponds to the coil at the smallest radial location. The other radial positions increment from 1 to 10 progressively increasing in radius. The locations are given in Table 3.1 where R_W/R_C is the ratio between the radial location of the wire and the channel centerline, respectively. The locations are based on physical measurements with an error of ±0.1mm.

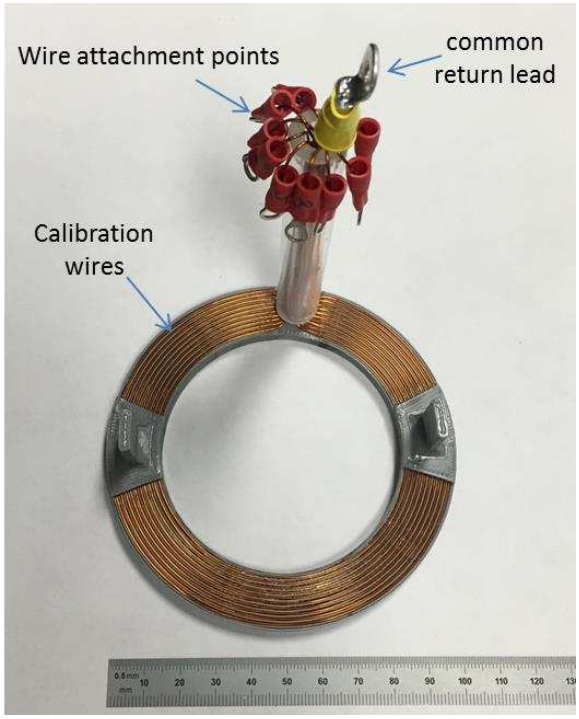

Figure 3.9: Hall current sensing calibration coil for CSU HET.

Table 3.1: Calibration wire locations normalized by channel center line with respect to thruster center axis.

Coil #	1	2	3	4	5	6	7	8	9	10
R_W/R_C	0.856	0.888	0.919	0.951	0.983	1.014	1.046	1.077	1.109	1.141

The calibration coils are controlled using a custom-designed switching relay box and a DC power supply capable of outputting up to 30A. The coils are then placed inside the ceramic channel of the HET at the desired axial location, as shown in Figure 3.10. The use of 3D printed spacers that sit between the anode and the coils allow for accurate control of the axial position.

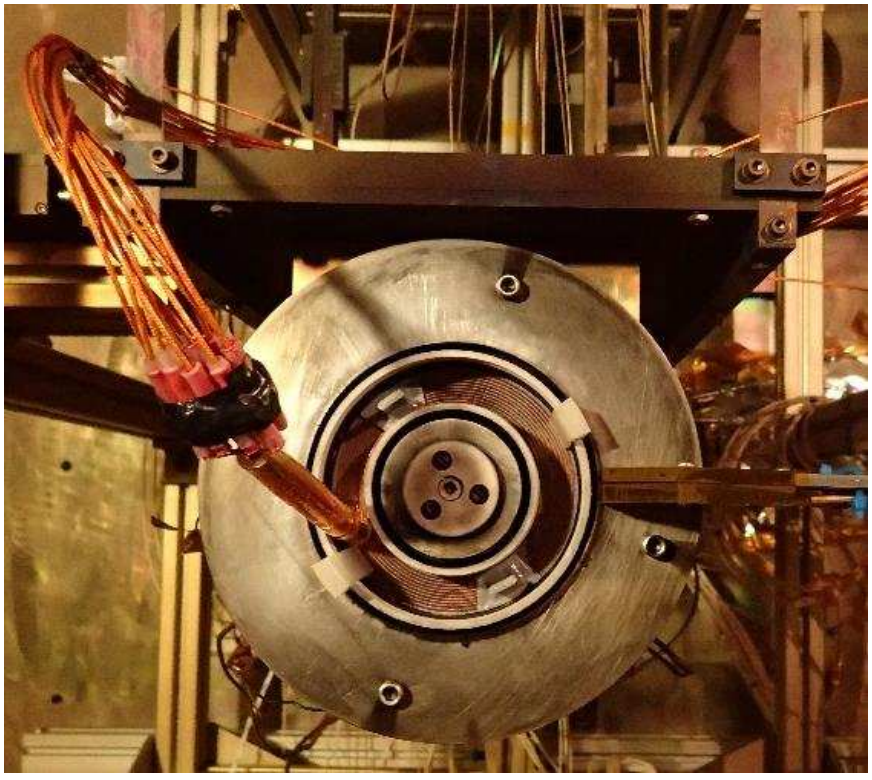

Figure 3.10: Calibration coils placed inside the CSU HET during calibration. The eight sensor array is located at the 3 o'clock position outside the channel.

The thruster inner coil and outer coils are energized and powered through the entire calibration process while a current was applied to each calibration wire. A background

measurement was first acquired for each axial position of the calibration coils, where only the thruster outer and inner coils are energized. The axial location of the coil was set using one of eight spacers that rested between the anode and the calibration coil, given in Table 3.2.

Table 3.2: Axial calibration locations normalized by channel length with 0 and 1 corresponding to the anode surface and channel exit, respectively.

Axial Pos.	1	2	3	4	5	6	7	8
Z_W/L_C	0.290	0.419	0.545	0.675	0.804	0.932	1.058	1.184

A LabVIEW program recorded the output voltage of the sensor as each wire had current applied, as described in the previous section. For the 10 wire calibration coil, a measurement for one single sensor at one axial location would look similar to Figure 3.11. Each step in Figure 3.11 represents applying current to one of the radial wires. The first radial wire was located near the inner channel wall, furthest from the sensor. The largest step corresponded to the wire nearest the outer channel wall, and therefore, closest to the sensor. The increase in the sensor output as the source of the induced current nears the sensor was as expected. The voltage decreased each time a coil was charged. The resistance of the sensor increased due to the induced field and the voltage drop across the passive resistor decreases, respectively.

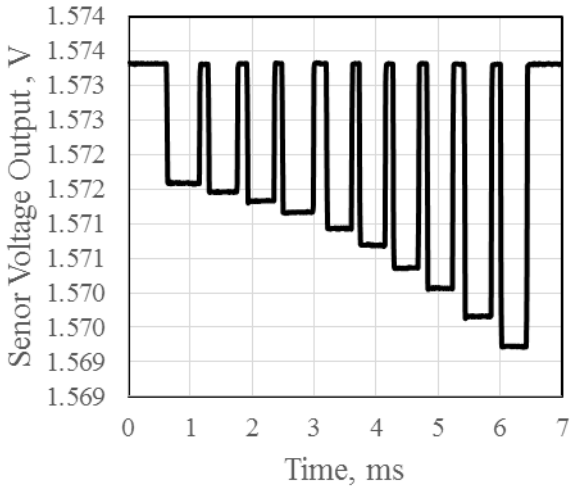

Figure 3.11: An example of the voltage drop measured across a sensor for a fixed axial calibration location as each of the 10 radial coils are energized individually.

In the case of the two-axis probe, the calibration must be repeated for each measurement position. Ideally, the coils were placed at an axial position and then the two-sensor array probe was placed at the first measurement position. The radial coils were then cycled as the outputs of the two sensors were recorded. The sensor was then moved to the next measurement location and the process was repeated. This continues for all of the desired sensing locations; four in the case of our experiments. The coil assembly was placed at the desired number of axial locations to fully map the field. The eight sensor array allowed for a simplified process. Since all eight sensors are already at the desired measurement locations and they are sampled simultaneously, the calibration coils only need to be moved for each axial location. The calibration data were then used to create the Green's matrix in the same way as described in the simulated calibration section.

3.4.3. Inverse Solution

The calibration process has the sole purpose of generating the A matrix shown in Eq. (2-4) for the inverse problem. A MATLAB script was written using the "fmincon" function to execute the constrained minimization algorithm and solve Eq. (2-4). The current density solution obtained was a row vector of length equivalent to the number of radial calibration coils multiplied by the number of axial calibration locations. This vector was then reshaped, inversely to how each row of the Green's matrix was created, to obtain a contour plot of the current distribution. The regularization term, λ, determines the amount of second order smoothing applied to the current density distribution, as previously described in the inverse magnetostatic section. The inverse solution process is set to solve the problem over an even space logarithmic range of regularization parameters. A small regularization value can lead to a solution that is discontinuous and not representative of a realistic distribution. Too large

of a regularization parameter can lead to an abundance of smoothing and yield a generic bell-curve distribution, sacrificing resolution of fine features in the solution. An example of these extremes is shown in Figure 3.12 and Figure 3.13. The optimal amount of regularization is chosen by programmatically finding the location of maximum curvature along the L-curve plot.

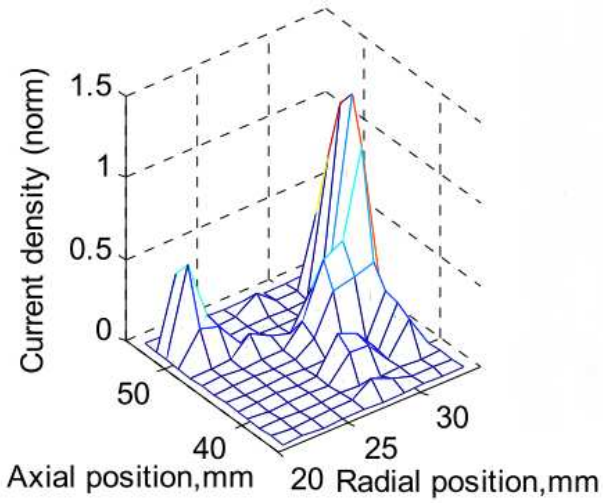

Figure 3.12: Too small of a regularization parameter resulting in a discontinuous solution. Reproduced from Fig. 3.20a of Ref. [17].

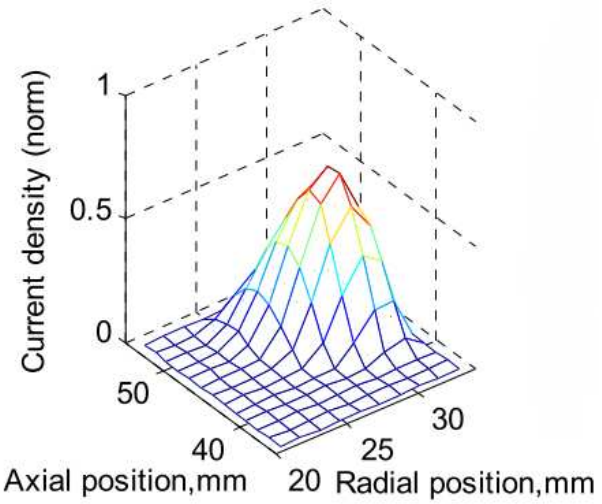

Figure 3.13: Too large of a regularization parameter resulting in an over smoothed solution. Reproduced from Fig. 3.20c of Ref. [17].

There were three different ways the data were processed, the full time-averaged solution, the calibration averaged solution, and the measurement averaged solution. Each data process method yielded unique information about the problem.

The full time-averaged method was the first attempted solution method for all of the data. For both the calibration and testing measurements, 200,000 samples are acquired in 0.1 seconds at a rate of 2 MHz for each sensor. With eight sensors that results in 1,600,000 data points for a single test measurement, with an equivalent amount for the background measurement. An example of the basic linear problem for our system is shown in Figure 3.14

where *A* is the Green's matrix created from calibration, *J* is the current density solution vector that is being found, and *B* is the change in magnetic field measured by the sensors during testing. The third dimension represents the raw data containing 200,000 samples that are acquired during calibration and testing. For the time-averaged method both the *A* matrix and the *B* vector are averaged through the third dimension to obtain two dimensional matrices.

$$\left[\left[\begin{matrix} A_{1,1} & \cdots & A_{1,80} \\ \vdots & \ddots & \vdots \\ A_{8,1} & \cdots & A_{8,80} \end{matrix}\right]\right] \left[\left[\begin{matrix} J_{H_1} \\ \vdots \\ J_{H_{80}} \end{matrix}\right]\right] = \left[\left[\begin{matrix} B_1 \\ \vdots \\ B_8 \end{matrix}\right]\right]$$

Figure 3.14: Representation of linear magnetostatic problem in 3 dimensions. The third dimension represents time.

The solution process is then applied to this averaged data to obtain an average solution and an optimal regularization parameter for this solution. The results from this routine are the time-averaged solutions presented later.

The second solution method only averages the calibration matrix for the solver. In this case, the *B* vector still has a length of 200,000 values in the third dimension. The regularization parameter determined from the full time-averaged solution is used to solve the inverse problem for either a section or all of the 200,000 measurements made. The fluctuations present in the measurement vector, *B,* are due to fluctuations in the magnetic field due to the Hall current as well as plasma and environmental noise induced into the sensor system. The results from this routine are referred to as the temporal solutions in a later section.

The third solution method averages the *B* vector and solves the inverse solution using the time-averaged regularization parameter. The calibration matrix is not averaged and

therefore has a length of 200,000 in the third dimension. The solution, J_H, vector can then be analyzed to determine the error due to environmental noise. The idea is that any fluctuations picked up during the calibration method are due only to environmental effects. Therefore, by solving for the J_H vector using the raw data from the calibration matrix, all of this noise is propagated into the solution vector, as described by Monte Carlo error analysis [38].

To summarize, the regularization term was determined from the calibration process using sample-averaged data. The same regularization term was then used to determine current density from a section of the raw measured magnetic field data, sampled at 2 MHz. This process takes significant computational time (~10 hours for 50,000 data points) but provides temporally varying 2D images of the Hall current structure within the thruster channel. The results from these solutions with the thruster under different operation conditions will be presented in the next section.

4. Testing and Results

Several tests were run using both the probe and array prototype sensors. Due to time constraints less testing was done with the probe system. The majority of the results will focus on the measurements made using the eight sensor array. This chapter will first cover the probe results and then continue on to the array measurements. The presentation of these results aims to document the Hall current sensor development process and demonstrate the current capabilities of the system.

4.1 Two Axis Probe Testing

Preliminary testing with the moving probe that contained one radial and one axial sensor quickly made it clear that the initial orientation of the probe was too invasive to the thruster plume. During the design of the probe the stainless steel end cap of the probe was made to be only 1.27 mm thick to minimize the gap between the sensors and the front pole face. The orientation had the center axis of the probe tube parallel with the thruster center axis. The rendering shown in Figure 4.1 shows how this orientation directly interfered with the thruster plume. The mounting bracket was redesigned to allow the sensor to approach the thruster radially from the side thus minimizing interference with the plume.

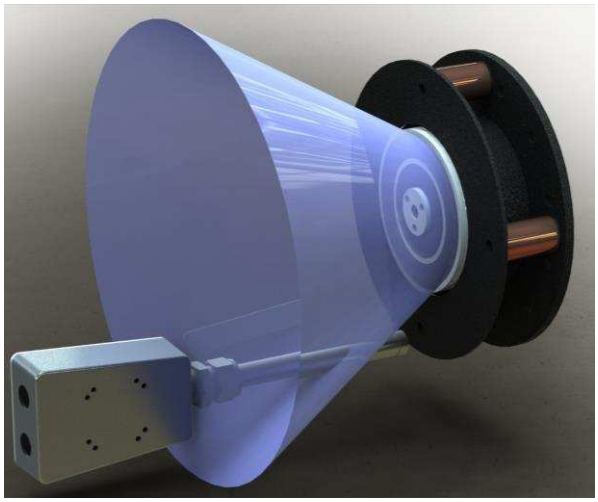

Figure 4.1: Rendering of original two axis probe position in front of CSU HET.

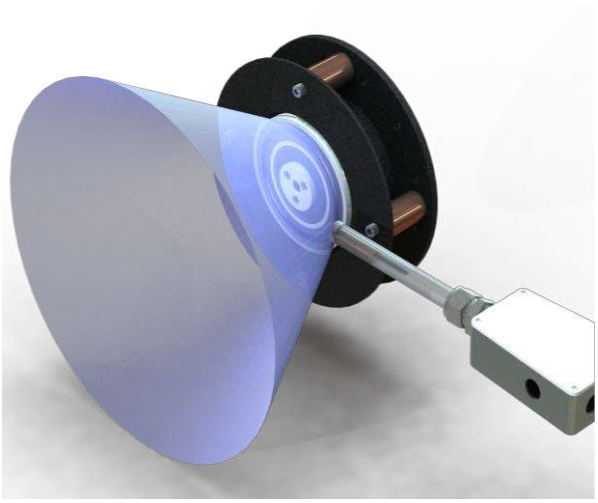

Figure 4.2: Rendering of improved sensor positioning to allow insertion of the sensor from the side of the thruster rather than in front of it.

Two separate tests were conducted with the sensor probe. The thruster was run at 1.5 kW using the center mounted cathode and the following details were used for both tests. The magnetic circuit used an inner coil setting of 5.5 A and an outer coil setting of 8.0 A. The calibration was performed before pumping down as detailed in the earlier sections, but only five axial positions were used during calibration. The coils were left on and once the chamber was pumped down the probe was cycled through the four of the eight measurement points shown in Figure 2.5, the two closest radial positions to the pole face and the closest and the furthest axial point. At these locations a background reading was acquired. The thruster was started and conditioned before testing to allow the HET to reach a stable operating point. The probe was then moved to each of the four positions as quickly as possible and the

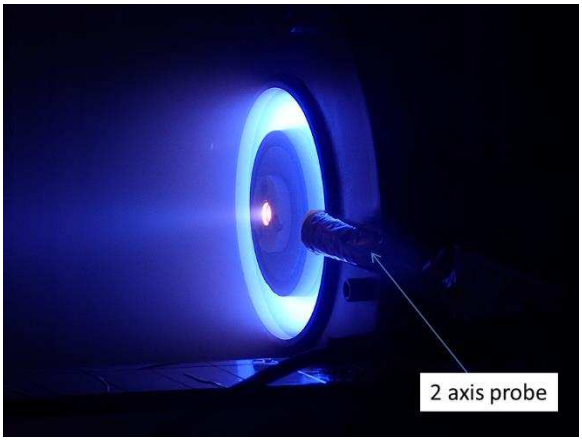

Figure 4.3: Two axis probe taking measurements on the CSU HET running at 1.5 kW.

measurements were recorded, as shown in Figure 4.3. The positions nearest to the channel caused a slight perturbation in thruster operation, but the change in the discharge current and cathode to ground voltage were both less than 2%. A major source of error during testing was the positioning of the probe relative to the thruster. An optical limit switch was attached to the backplate of the thruster to provide a reference for all of the stage movement. Although care was taken to home the stage, there is a large amount of uncertainty in positioning that was propagated into the solutions, and the first test yielded unsatisfactory results. Special care was taken in the setup of the second test to assure that the positioning references were as accurate as possible.

The nature of the probe system only allowed for time-averaged solutions because there was a lapse in time during movement of the sensor to different positions. As such, all of the 200,000 data samples from each measurement position during testing and calibration were averaged. Each position was treated as a separate sensor measurement in the setup of the inverse problem and therefore made up one of the four rows in the Green's matrix, *A*, and the magnetic field vector, *B*. The results from inverse solution of the test data are shown below.

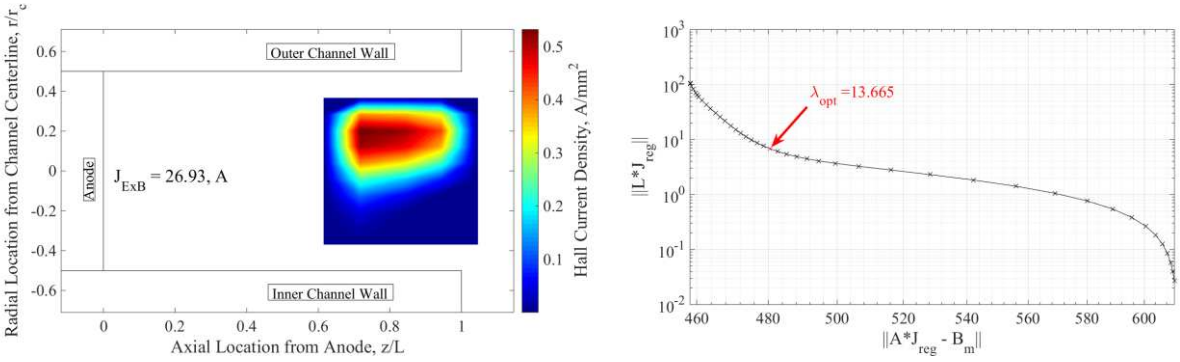

Figure 4.4: Time-averaged smoothed contour plot of the Hall current density

distribution in the CSU HET operation at 1.5 kW and 4.89 A discharge current on Kr.

Figure 4.5: L-curve plot used to obtain the optimal regularization parameter for the solution shown in Figure 4.4.

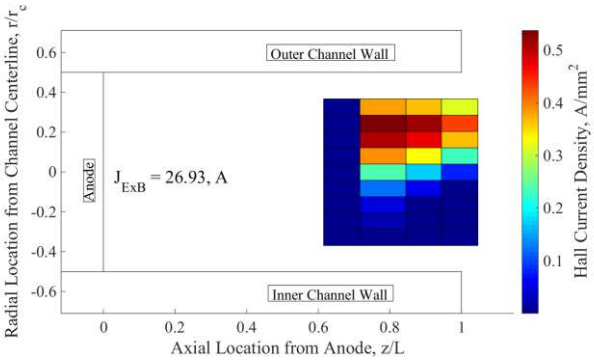

Figure 4.6: Gridded plot of same solution as Figure 4.4 to show the resolution. The blue border on the bottom and left of the solution domain is an artifact of the MATLAB plotting tool.

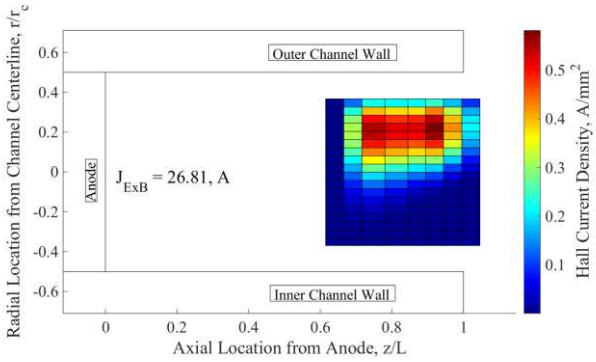

Figure 4.7: The same test data but the Green's matrix is interpolated before being passed to the inverse solver. Shows an increase in resolution without significant modification to the solution.

In Figure 4.4 to Figure 4.7 the Hall thruster channel is shown with normalized dimensions and the thrust plume is leaving the thruster to the right. The total Hall current is displayed as well as the distribution of the current density. The results showed the Hall current density significantly shifted towards the outer channel wall rather than being more centrally located as expected. It is possible that this shift was due to the layout of the radial magnetic field in the channel. In Figure 4.4 the solution was plotted using a filled contour function. The resolution of the data was poor due the low number of calibration positions, as illustrated in Figure 4.6 with the gridded plot. The variation of size in the axial grids was due to the inaccuracies in the printing of the axial spacers, therefore slightly varying the axial locations such that they weren't equally spaced. The solution was modified by interpolating the Green's calibration matrix with a spline curve prior to solving the inverse problem. Figure 4.7 shows how the resolution was increased without significantly modifying the total

Hall current or the overall distribution. In the gridded plots the blue zones on the bottom and left of the solution domain are artifacts of the surface plotting tool used.

These initial results were meant to verify the solution and calibration processes before progressing to the final prototype. During the execution of this testing several error sources were identified. The most notable being the lack of repeatability in sensor positioning due to the translation stage errors. The temperature reading of the sensors was also unreliable due to large amounts of induced noise from the plasma. At one point the probe temperature was observed to be around 80°C and close to the temperature limit of the plastic SOIC-8 package. There was also concern about the sensitivity of the sensors varying significantly between calibrations and testing due to temperature differences causing solution errors. These sources of error were eliminated in the eight sensor array design described next.

4.2 Eight Sensor Array Testing

The sensor array was tested with the CSU Hall thruster under several different operating conditions. All of the tests took place using Krypton as the propellant with future goals of testing with Xenon as well for comparison. There were two different configurations for the mounting of the sensor. In once configuration we mounted the sensors directly to the fixed frame of the thrust stand in a position near the thruster. It was assumed that the distance that the thruster would move during operation would be minimal and have no significant effects on the solution. This allowed for thrust measurements to be made during testing. This configuration is referred to as the separated configuration. The other configuration, called the fixed configuration, mounted the sensors directly to the thruster ensuring the relative distance between the sensor and the thruster did not change during

testing or calibration. This configuration did not allow for thrust measurements due to the stiffness of the Triax cabling and the water lines attached to the eight sensor array.

4.2.1. Separated Configuration

In this configuration the sensor was mounted to the fixed frame of the thrust stand and not the thruster, and was used for the majority of the testing. The goal was to still be able to obtain thrust data during testing and then make a comparison to the thrust calculated by integrating the product of the measured Hall current density and the radial magnetic field, as shown in Eq. (1-5). The nine Triax cables were run along one of the extruded aluminum struts with the water cooling lines left free hanging as shown in Figure 4.8 below.

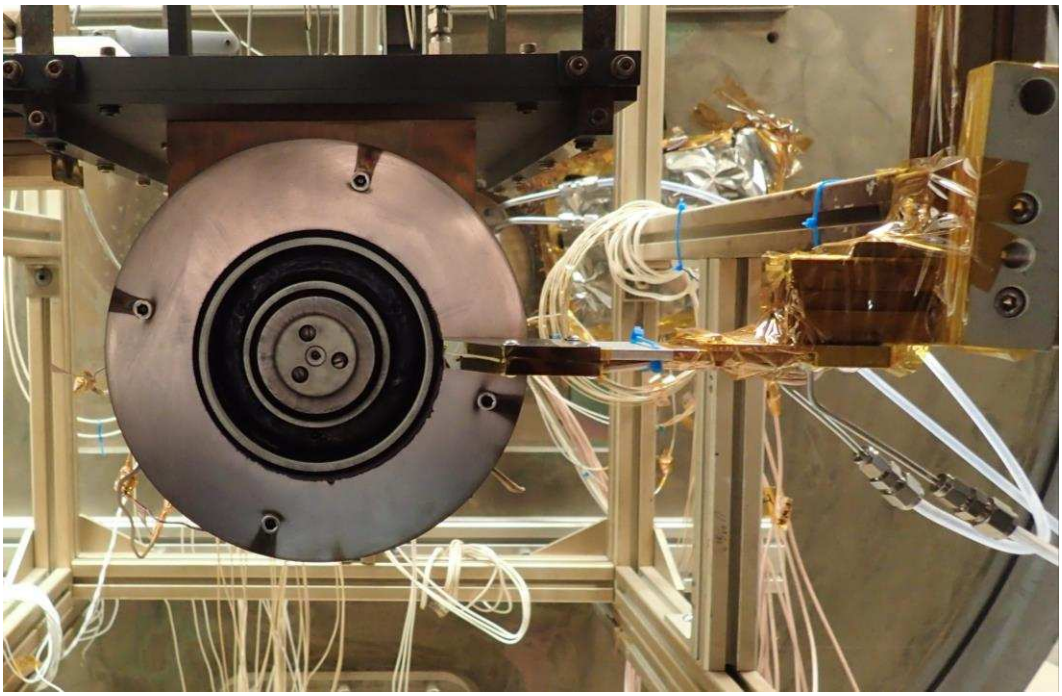

Figure 4.8: 8 Sensor Array close testing setup. The position shown here is the closest radial mounting point that was tested.

A summary of all of the testing conditions presented in this section are presented in Table 4.1. There were some testing cases where the high bandwidth discharge current measurement system was not functioning and therefore no breathing mode frequency was

obtained. The frequencies that are shown in the table were calculated from voltage measurements across a shunt wired in series with the cathode power line. The error is ±1 kHz. At lower discharge voltages it was more difficult to discern the breathing mode frequency from the noise floor. The far position refers to testing with an external cathode with the eight sensor array mounted as shown in Figure 4.9, and these tests displayed a direct correlation between discharge voltage and breathing mode frequency. This trend has been observed in previous work [39]. The reported thrust values have a maximum error of ±2 mN for the tests shown.

Table 4.1: CSU operating telemetry recorded during testing with the sensor array isolated from the thrust stand with the test numbers indicated on the left hand side of the table. †Indicates the tests that were conducted with the external cathode.

		Power [kW]	V_D [V]	I_D [A]	$\dot{m}_a$ [mg/s]	Thrust [mN]	Breathing Mode Frequency [kHz]
Close Position	1	1.33	275	4.85	3.7	48.0	N/A
	2	1.55	300	5.16	4.0	67.3	31.8
	3	1.64	300	5.46	4.0	59.9	N/A
	4	2.22	300	7.41	5.5	93.9	N/A
Far Position†	5	1.53	250	6.11	3.5	72.0	26.0
	6	1.54	275	5.51	4.3	69.1	29.0
	7	1.53	300	5.10	4.0	63.1	32.1
	8	1.54	325	4.75	3.7	63.2	N/A

The anode flow rates are given in Table 4.1 and the cathode flow rate was maintained at 10% of anode flow rate.

The test sets were divided into two major categories describing the general location of the sensor radially relative to the channel. The close position had the fixture holding the eight sensor array slightly in the plume during operation as shown in Figure 4.8. The internal electride cathode was used for the close position tests while the external porous tungsten-impregnated cathode was used for the far position testing, shown in Figure 4.9.

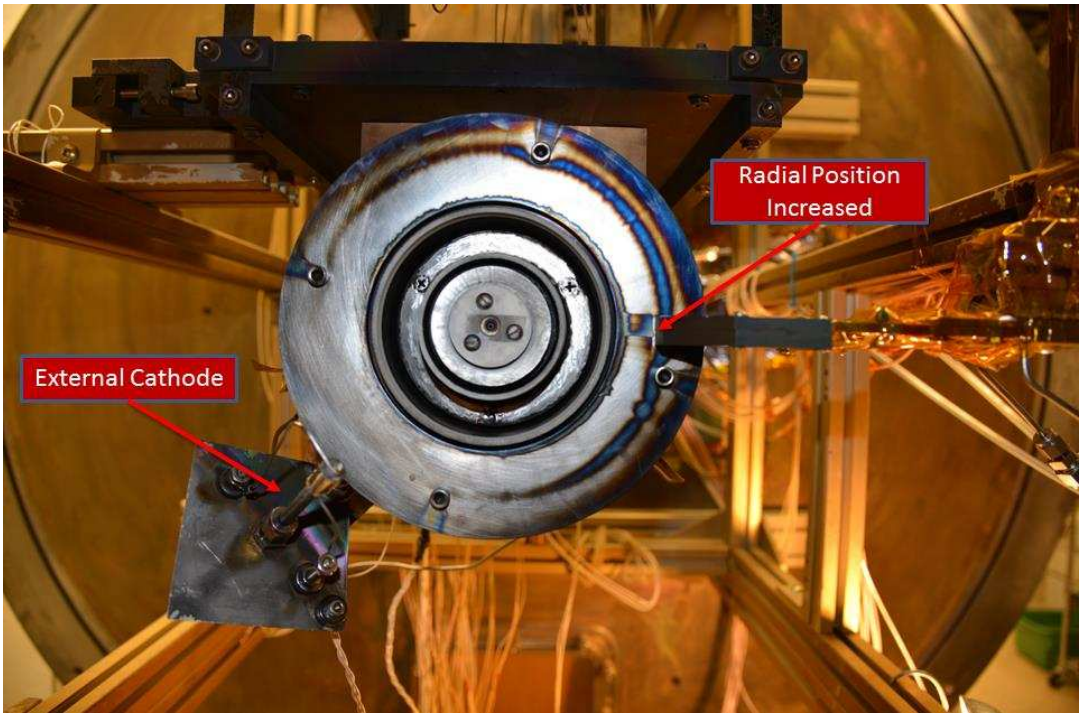

Figure 4.9: Eight Sensor Array far testing setup. The position shown here is the furthest radial mounting point that was tested. The external cathode is shown at the bottom left of the image and was used for the tests conducted at this sensor array location.

As previously detailed, the average solution for each test needed to be calculated first in order to determine the optimum regularization parameter. The average solutions also provided insight into the overall location of the Hall current within the solution domain.

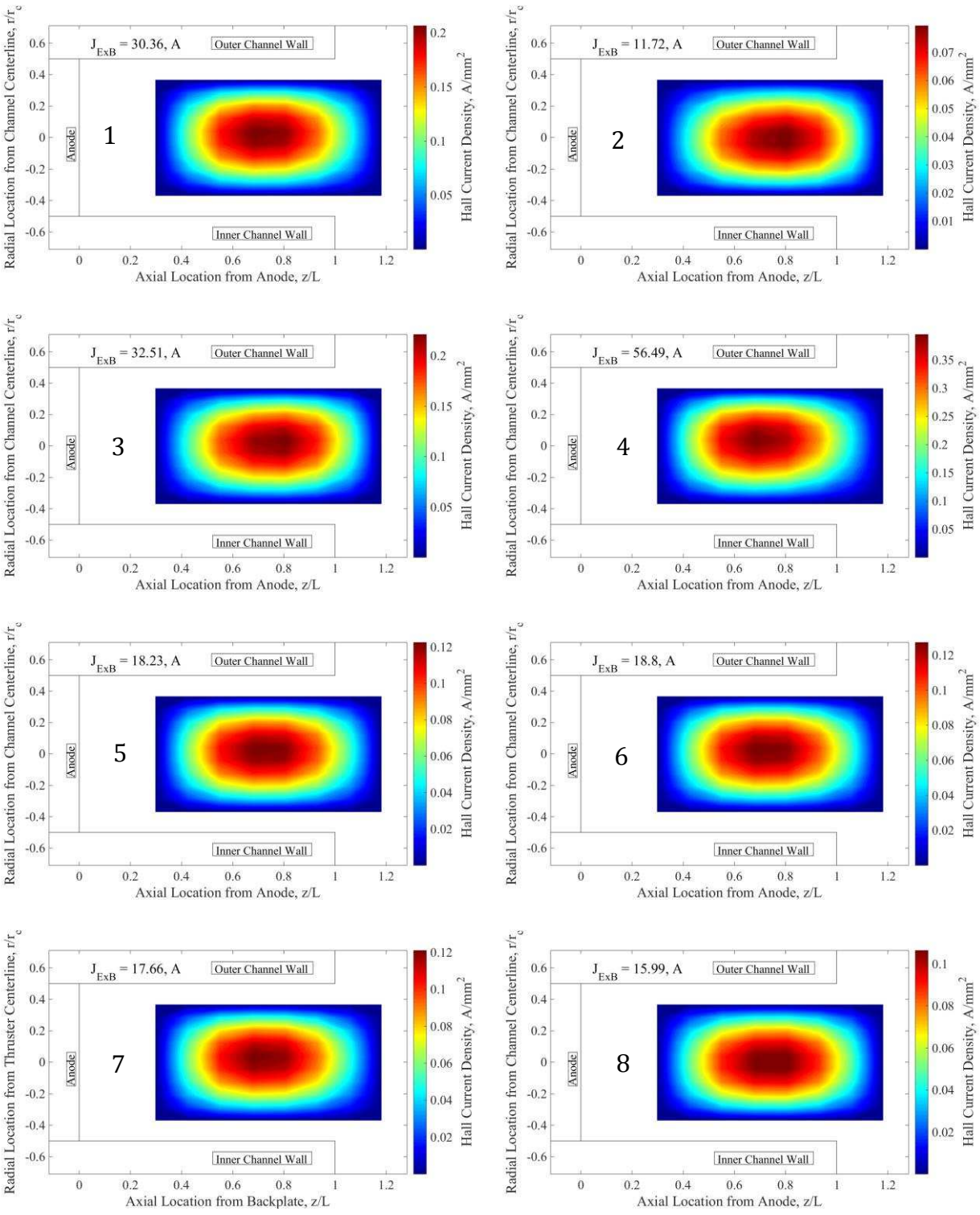

Figure 4.10: Average Hall current density solution plots with the anode shown at the left of the images and total Hall current displayed at the top. The figures are labeled 1 through 8 corresponding to the labels in Table 4.1

The data for all of the different test sets shown in Figure 4.10 shared a similar average distribution pattern, which is believed to be an artifact of the averaging technique. The Hall currents, displayed at the upper left corner of the images, exhibited an increasing trend as discharge current increased. The magnitude of the Hall current density for dataset 2 was lower than expected considering it was a similar operating point to dataset 7. During calibration the thrust stand was locked in place while the coils were moved and measured. The lock only mounted to one side of the thrust stand and it was not designed to be a hard lock so the thruster could move relative to the sensor slightly. If the thrust stand had shifted axially slightly during calibration, then an amplitude error could have been induced into the measurements while the overall distribution remained consistent. This error source was one of the reasons the sensor was attached to the thruster in future tests to ensure the relative spacing between the HET and the sensor did not change. All of the L-curves for the datasets were used to find the optimal regularization parameters, and they are summarized in Table 4.2.

Table 4.2: Optimized regularization parameters determined by the L-curve test for the eight datasets. The L-curve plots can be found in appendix A.

Test	1	2	3	4	5	6	7	8
λ_{opt}	84.493	97.748	63.130	73.034	74.717	63.130	88.995	44.215

Preferably, optimal regularization parameters would have been chosen for each of the 200,000 measurements, but due to computational constraints, a single optimal regularization parameter value from the averaged data was used. The data collected during the eight-sensor array tests above were acquired at a rate of 2 MHz and averaged to a frequency of 500 kHz to improve the signal to noise ratio. The calibration averaged solution

method was used on the datasets, but only some are displayed here for document length considerations.

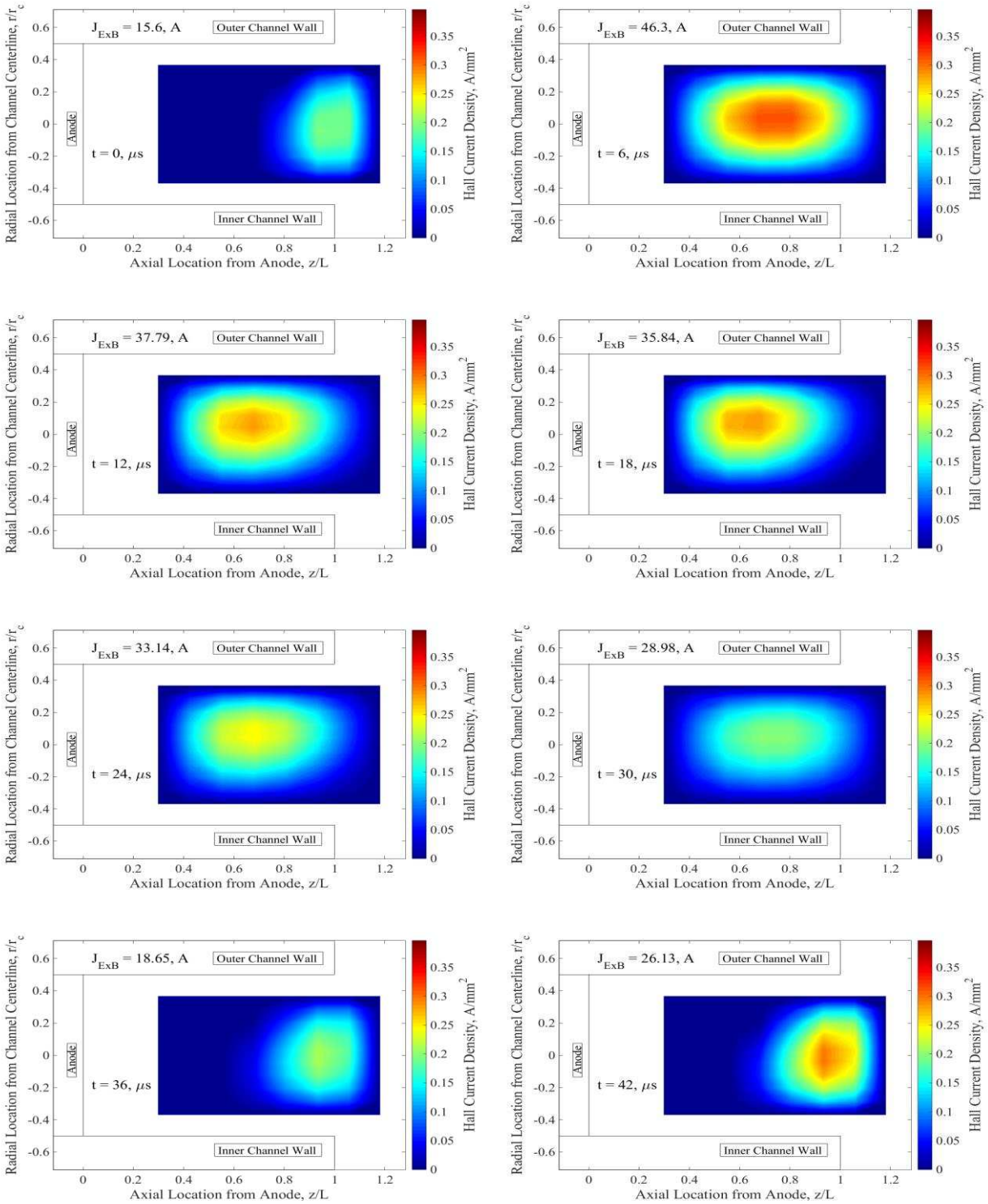

Figure 4.11: Temporal solution for CSU HET dataset 3 in Table 4.1, 6 μs between frames.

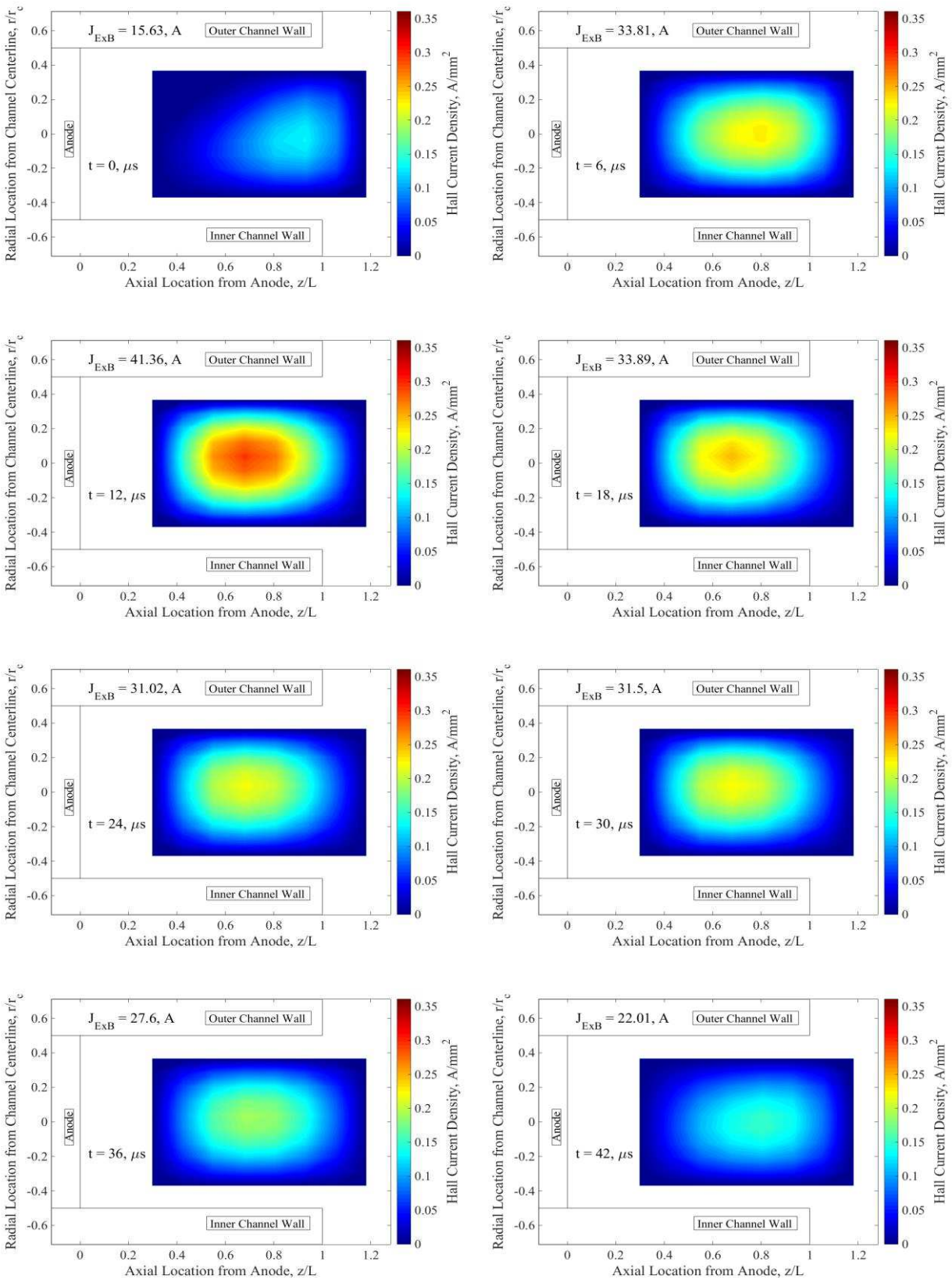

Figure 4.12: Temporal solution for CSU HET dataset 1 in Table 4.1, 6 μs between frames.

The dataset shown in Figure 4.11 was taken during standard 1.6 kW operation of the thruster with the center mounted cathode and a discharge voltage of 300 V. The series of images detailed a breathing mode cycle of the Hall current. The current density started to increase downstream near the channel exit. As neutrals filled the channel the electrons began to ionize the gas particles and the current density concentration moved upstream as more of the neutrals were ionized. As the majority of the neutrals inside the channel were ionized the Hall current density decreased. Once all of the ions were expelled and neutrals refilled the upstream section of the channel, the current moved back downstream towards the channel exit and the maximum radial magnetic field. The other set of images in Figure 4.12 were taken with the thruster operating at 1.3 kW with a lower discharge voltage of 275 V and reduced gas flow rate. The lower discharge voltage had the effect of decreasing the breathing mode frequency of the thruster and increasing the ionization region axially in the channel.

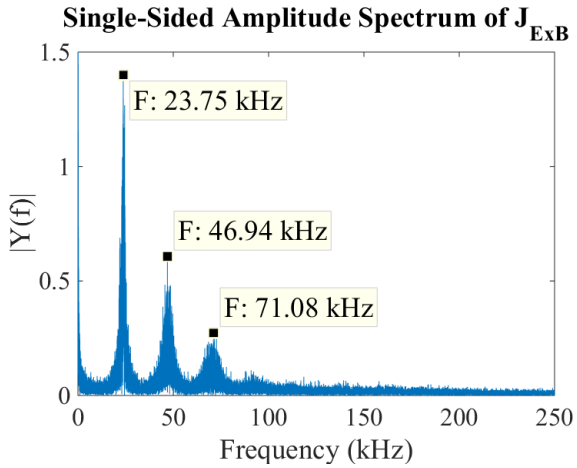

Figure 4.13: Spectrum analysis of the total Hall current data taken for dataset 3 operating at V_D = 300V.

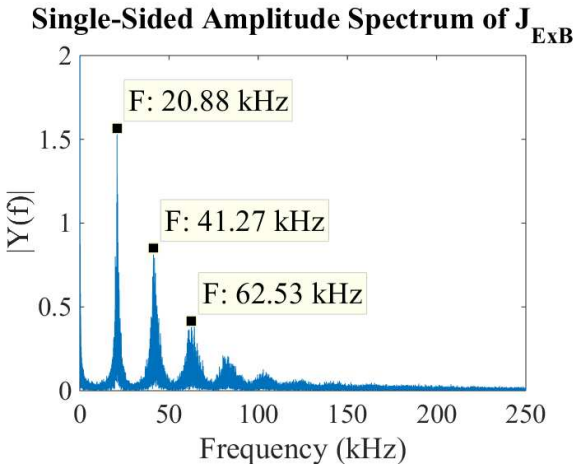

Figure 4.14: Spectrum analysis of the total Hall current data taken for dataset 1 operating at V_D = 275V.

A fast Fourier transform of the temporal Hall current amplitude was calculated and spectral power density plots are shown in Figure 4.13 and Figure 4.14. The breathing mode frequency for the 1.5 kW and 1.3 kW operation points was 23.75 kHz and 20.88 kHz, respectively. This decrease in the breathing mode was due to the lower discharge voltage setting as described previously and described in reference [39].

The radial magnetic field of the thruster channel was mapped using a FW Bell gaussmeter with a transverse probe. The probe was swept axially along the length of the channel at different radial positions from the inner wall to the outer wall. The maximum radial magnetic field along the centerline is located just downstream of the exit plane as shown in Figure 4.16. The ionization region has been shown in the literature to setup just upstream of this point see reference [10] for example.

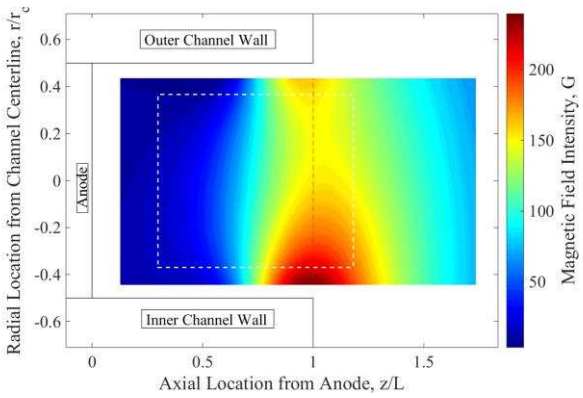

Figure 4.15: Radial magnetic field magnitude in Gauss for the inner coil set to 5.41 A and 7.94 A for the outer coil. This was the field setting for dataset 3. White box indicates solution domain for Hall current density.

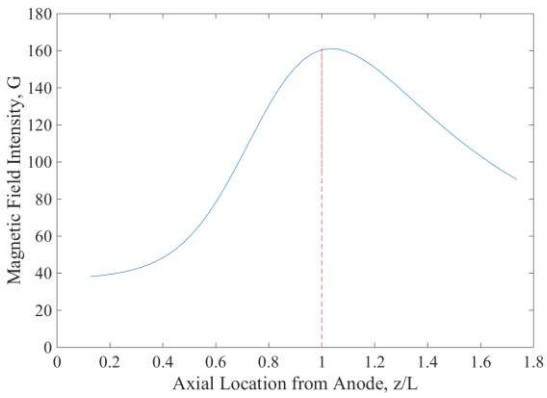

Figure 4.16: Radial magnetic field along the channel centerline for the settings in dataset 3. The red line indicates the channel exit.

The Hall current density and the radial magnetic field, shown in Figure 4.15, were assumed to be the same azimuthally around the channel. The two arrays of values were then multiplied together and integrated over the channel volume to obtain the thrust. These

values were compared to the value measured by the thrust stand for dataset 3. The radial field contour was interpolated at the solution points of the Hall current density contour. The field values were multiplied with the temporal measurements and solutions for the Hall current density. The thrust matrix was then averaged to obtain an average thrust for the entire measurement time. A thrust value for the averaged solution of the Hall current density was also calculated for comparison. The average thrust from the temporal solution was 77.1 mN ±18% and the averaged solution predicted a thrust of 73.2 mN ±21%. The thrust stand recorded a value of 59.9 mN ±1.6% during the sensor measurement. This yielded a difference of 22% between the predicted and recorded thrust values when using the thrust stand value as the basis. The alignment and offset of the gauss probe and the calibration coils for the Hall current sensor were both sources of error for the calculations of the total thrust. A 1mm shift downstream of the radial magnetic field values caused a 5 mN change in the predicted thrust. This finding stresses the importance of positioning of the sensor systems and gaussmeters for collecting data used to calculate the thrust.

4.2.2. Fixed Configuration

In an attempt to reduce the relative positioning errors during calibration of the Hall current sensor, the array was mounted directly to the thruster. This configuration did not allow for measurement of the thrust using the thrust stand due to the stiffness of the eight sensor array wires and cooling lines. Consequently, these tests focused on investigating the correlation between the sensor measurements and the discharge current oscillations. Extruded aluminum struts were used to create a linkage between the sensor and the thruster backplate, as shown in Figure 4.17. Tests were conducted with the internal and external cathodes and datasets from both are included in this section. The sensor array was located

in the closer position of the two previously discussed, also shown in Figure 4.17. It was determined that this position yielded better results due to its proximity to the channel and therefore the Hall current during operation. Data were taken with the thruster operating with the internal and external cathode.

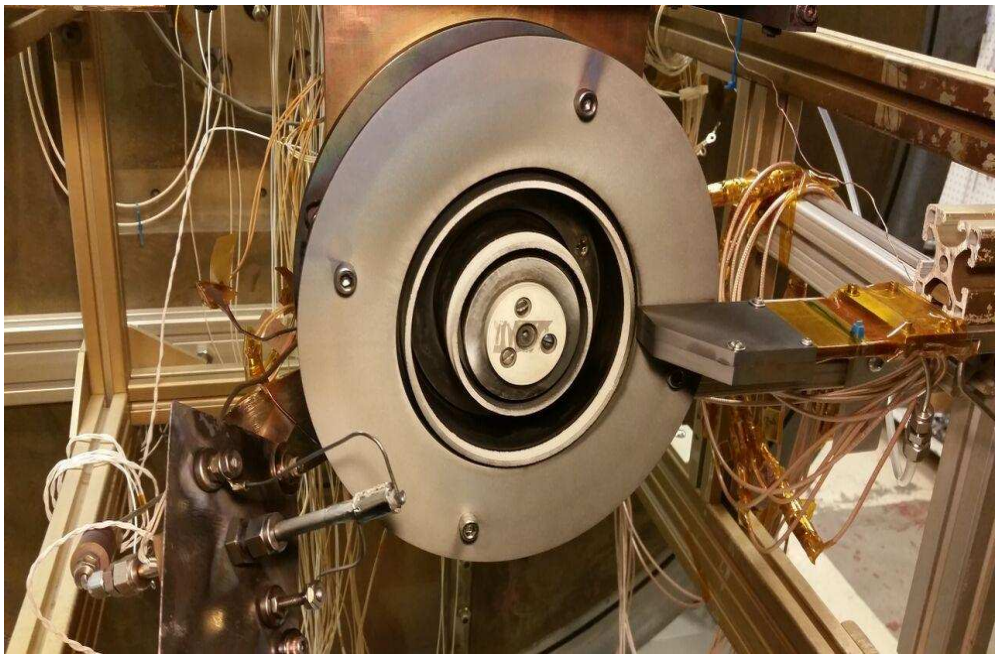

Figure 4.17: Testing configuration where the Hall current sensor was attached to the thruster backplate to fix the relative position of the system.

An overview of the operational settings of the thruster for each dataset is shown in Table 4.3. The cathode flow was once again not optimized and instead was set to 10% of the anode flow rate for all testing. Also, there was no thrust data available so they are not displayed in the table. The first 3 datasets, shown in Table 4.3 used the internal electride cathode while the last 3 used the external cathode.

Table 4.3: CSU operating telemetry recorded during testing with the sensor fixed to the thruster with the test numbers indicated on the left hand side of the table. †Indicates the tests that were conducted with the external cathode.

	Power [kW]	V_D [V]	I_D [A]	$\dot{m}_a$ [mg/s]	Breathing Mode Frequency [kHz]
1	1.10	300	3.61	3.0	24.4
2	1.55	275	5.62	4.3	26.7
3	1.55	300	5.16	4.0	28.5
4†	1.08	300	3.60	3.0	22.3
5†	1.53	300	5.10	4.0	31.0
6†	2.16	300	7.19	5.0	35.3

Datasets 1 to 3 were all taken during the same day of testing using the internal cathode, as shown in Figure 4.18. Each of the three datasets were recorded after the CSU HET had reached a stable operating point and the magnetic field was optimized to minimize the discharge current. The last three datasets were also taken during the same day of operation. These three tests kept the discharge voltage the same while varying the mass flow rate and thereby the operating power level of the thruster. The breathing mode frequency was once again determined from a spectral analysis of the discharge current. An increase in the breathing mode frequency was observed as the power was increased, as expected from the literature [39].

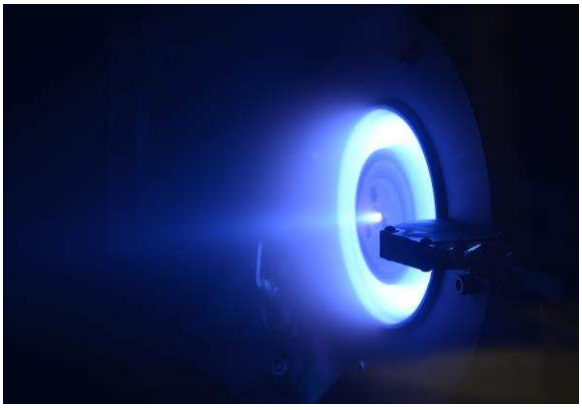

Figure 4.18: CSU HET operating with and internal cathode during testing of the eight sensor array.

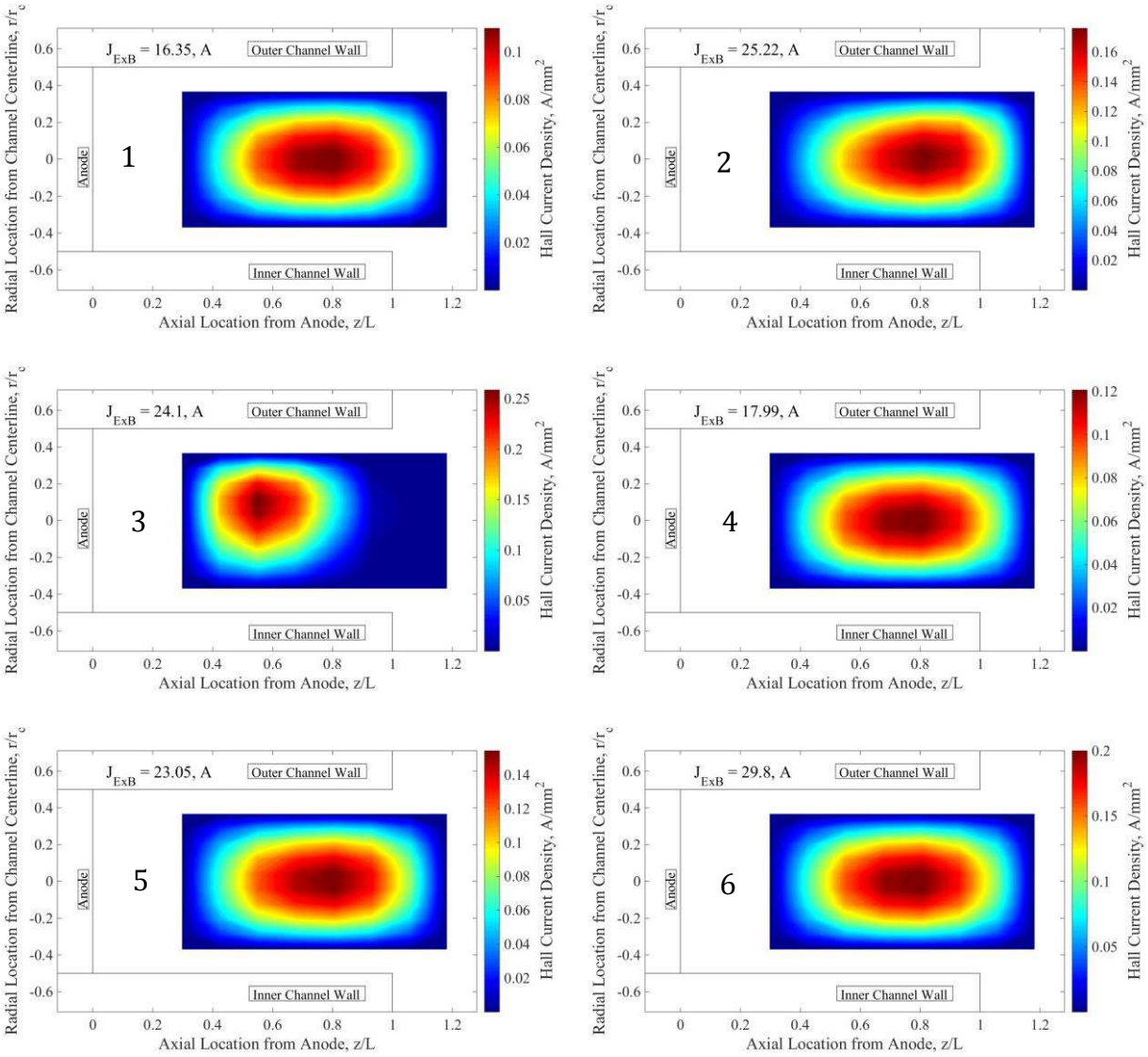

Figure 4.19: Average Hall current density solution plots with the anode shown at the left of the images and total Hall current displayed at the top. The figures are labeled 1 through 6 corresponding to the labels in Table 4.3.

Similar to the previous tests, the average solution method was applied to obtain a single optimal regularization parameter for each dataset in Table 4.3. All of the Hall current values for the datasets showed an increase in magnitude as the discharge current increased. The distribution was similar for all the datasets with the exception of dataset 3, which showed the Hall current more localized and upstream compared to the others.

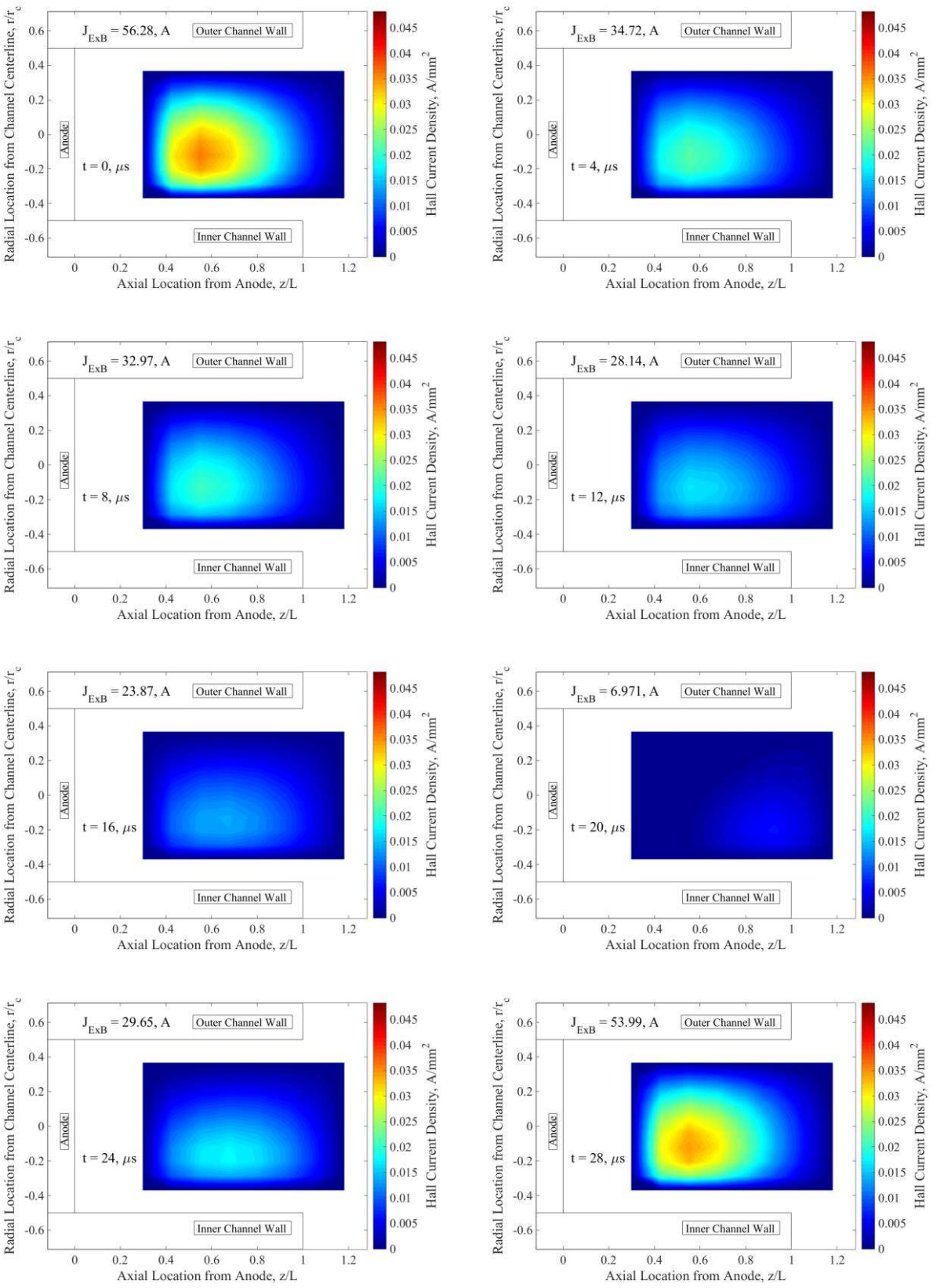

Figure 4.20: Temporal solution for dataset 6 in Table 4.3 with CSU HET 2.16 kW.

The time-resolved solution for the 6th dataset, Figure 4.20, exhibited a fundamental frequency of 37.2 kHz as can be seen in the movement of the Hall current distribution between the 4 μs interval frames. The same breathing mode motion as observed in the previous measurements was apparent but with higher variation in current density between frames. The Hall current varied from 1 to 10 times the discharge current in dataset 6. The sixth frame in Figure 4.20 (t = 20μs) corresponds to a Hall current with a magnitude ratio near unity with respect to the average discharge current, which is lower than ratios for datasets shown earlier. The Hall current density shifted toward the inner channel wall, which is also different from our previous results. The choice of the optimal regularization parameter had a large effect on the solution. Calculating the optimal parameter for every solution time frame, however, could improve the solution, but this was outside the scope of this work due to its computationally intensive nature. A comparison of the discharge current and the calculated Hall current is shown in Figure 4.21, and it demonstrates the positive correlation between the discharge and the azimuthal current, although the azimuthal current is relatively noisy. The calculated fundamental frequencies between the two currents only varied by 2 kHz and can be seen in the major Hall current oscillations amongst several secondary variations shown in Figure 4.21.

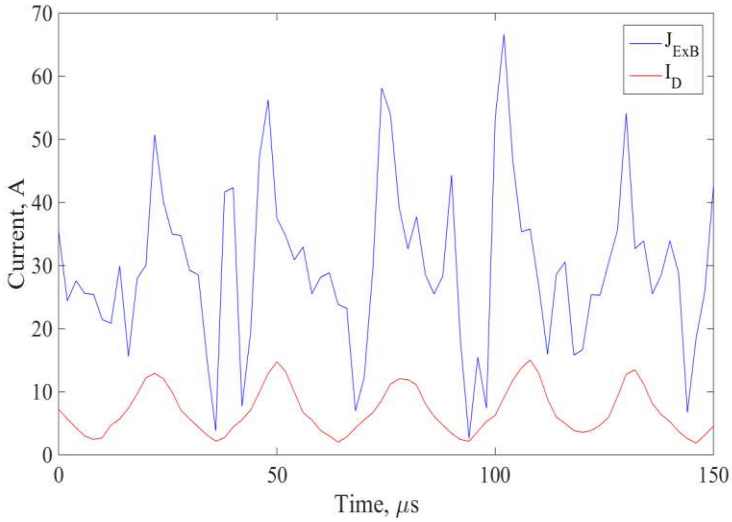

Figure 4.21: Hall current plotted against discharge current for dataset 6 over a span of 150 μs.

5. Conclusion

The sensor system presented in this thesis has demonstrated the ability to non-invasively resolve the time-dependent Hall current density distribution within a Hall effect thruster (HET). A probe and stationary array design were presented along with initial testing results. The use of commercially available tunneling magnetoresistive (TMR) sensors allowed the sensing of small magnetic field changes in a high intensity background magnetic field. The simplest approach was shown to utilize the space downstream of the front outer pole piece to sense the induced magnetic field due to the azimuthal current in the thruster channel. A Finite Element Method Magnetics (FEMM) simulation model of the CSU 1.5 kW HET was used to select the sensor locations to maximize the amplitude of the induced field seen by the sensors. A custom designed circuit and actively cooled casing was designed in this work to house the sensors. A graphite cover was utilized to reduce sputtering due to ion bombardment. Triax cabling and an embedded battery power source were both used to minimize the amount of environmental noise which is important to reduce solution error due to the ill-posed nature of the inverse problem. Testing of the sensor system with a double hanging pendulum thrust stand with a resolution of ±0.5 mN allowed comparisons to be made between calculated and measured thrust. The sensor system predicted the thrust generated by the HET to be %22 greater than the value measured by the thrust stand with 95% confidence. Comparison of measurements of the thruster discharge current to calculated temporal Hall currents verified that the sensing system imaged the Hall thruster breathing mode cycle with both data sources exhibiting equivalent fundamental frequencies ranging from 20 kHz to 32 kHz over the tested operating points of the thruster.

5.1 Future Work

This thesis has demonstrated the first successful experimental attempt at creating a non-invasive inverse magnetostatic Hall current density sensing system. The full ability of the system has yet to be shown until further characterization and testing can be accomplished. The remainder of this section provides ideas and goals for improvement of the system as a laboratory diagnostic and a flight hardware device.

The improvements to the sensor system can be categorized by the following categories:

1. Expansion of the Inverse Magnetostatic Algorithm
2. Optimization of Calibration Tools and Processes
3. Sensor Positioning and Array Design Layout

5.1.1. Expansion of the Inverse Magnetostatic Algorithm

The algorithm used to solve the inverse magnetostatic problem was largely based on the work done by Rubin [17]. Several assumptions had to be made for a solution to be obtained and the zero-boundary condition had the most significant impact on solutions. The contour plots that displayed the Hall current distribution within the channel always exhibited a gap between the solution domain and the inner and outer walls, shown in Figure 5.1. This was due to the physical limitations of the calibration tool as well as the zero boundary conditions imposed by the solver. The calibration tool

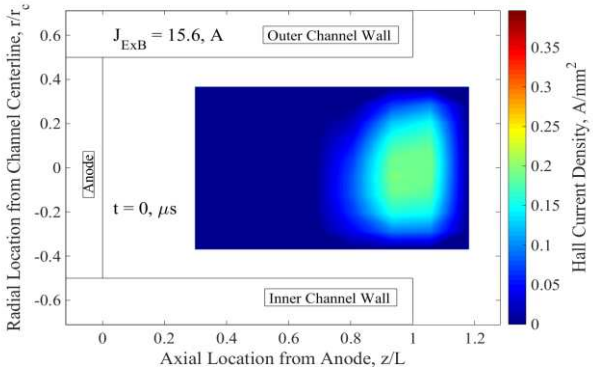

Figure 5.1 Example of Hall current solution contour measured during testing and solved for using the inverse magnetostatic algorithm.

described in chapter 3 has a thin wall that isolates the largest radial wire from the thruster channel. The wall was reduced to the smallest capabilities of the 3D printer used to create the holder. Even still, this offset can be seen in the contour between the solution domain and the walls. The zero-boundary condition would be valid if the solution domain had extended to the walls. As such, an improvement to the inverse solver could yield more accurate solutions. Modifying the boundary condition to force a linear condition rather than a zero condition could achieve a more accurate solution. Otherwise, extrapolation of the calibration data before generating the Greens matrix could extend the solution domain to the walls. A few attempts at this method were tested but at certain points an induced error of 15% resulted and it is suggested that more work be done in this. In Figure 5.1 the solution appeared to be compressed up against the boundary of the solution domain. The linear boundary condition and extrapolated calibration data would mitigate this, or further improvement could be made to the calibration system as described below.

5.1.2. Optimization of Calibration Tools and Processes

The current calibration method was described in detail in Chapter 3. The section detailed the use of a plastic holder that contained a single plane of equally spaced coils that fit into the thruster channel. Plastic spacers were placed beneath the coils to position them axially inside of the channel. Multiple spacers with varying thickness were used during a calibration for a given magnetic field setting of the thruster. The current applied to each calibration coil was controlled using a switching box from outside of the chamber. The calibration process consisted of fixing the coil at one axial location and then conducting the calibration measurement for each of the radial wires at that location. The calibration coils were then removed and the next largest axial spacer was placed inside the channel before

the calibration coils were re-inserted. This process was tedious and prone to error. An automated system that could be run in vacuum with the thruster at operating temperature would be ideal, but presents many system design challenges.

Currently, an improved design is being created that is in a tower configuration. The design is a single structure that contains all of the radial wires at all of the desired axial locations. In our first device there are 12 radial calibration positions and 10 axial calibration positions such that the tower contains 120 individual calibration coils. The circuit design of the system is optimized to minimize the number of relays needed to control the current to each coil. A script has been written to automate the cycling and measuring of the calibration current. This new system will allow the user to place the calibration rig into the thruster, start the process, and have it be completed in a matter of minutes. Further modifications to the materials used to house the calibration system would allow for the process to be carried out in vacuum while the thruster body is at temperature to reduce the error caused by thermal variances in the B-H curves of the magnetic materials used in the thruster. Currently we are waiting for funding to implement the first iteration of the tower calibration rig.

5.1.3. Sensor Positioning and Array Design Layout

In this study the sensors were placed outside of the thruster body to avoid significantly modifying the body of the thruster. If the sensors could be embedded into the outer walls of the channel the induced field seen by the sensors would be much larger while still not exceeding 30 G static field levels. In this location the temperatures of the channel, approximately 300-600 °C, prevent placement of the sensors. An active cooling system would be needed to maintain the sensors within a safe temperature range. With the recent advances in magnetically shielded thrusters the temperatures seen at the channel walls

could be low enough to satisfy the 150°C limit of the sensors. Otherwise, advances in 3D printing of ceramics could lead to cooled channel walls using heat pipe concepts, which would allow more arbitrary placement of sensors.

6. Bibliography

[1] K. E. Tsiolkovsky, *Collected Work: Vol. 2, Reactive Fflying Devices*. Izd. Akad. Nauk SSSR Moscow, 1954.

[2] D. Goebel, M. Martinez-Lavin, T. Bond, and A. King, "Performance of XIPS Electric Propulsion in On-orbit Station Keeping of the Boeing 702 Spacecraft," in *Joint Propulsion Conference & Exhibit*, 2002, no. July, pp. 1–4.

[3] M. Poole and M. Ho, "Boeing Low-Thrust Geosynchronous Transfer Mission Experience," El Segundo, 2013.

[4] A. I. Morozov, "The conceptual development of stationary plasma thrusters," *Plasma Physics Reports*, vol. 29, no. 3. pp. 235–250, 2003.

[5] R. R. Hofer, "Development and Characterization of High-Efficiency, High-Specific Impulse Xenon Hall Thrusters," University of Michigan, 2004.

[6] M. Sekerak, "Plasma Oscillations and Operational Modes in Hall Effect Thrusters," University of Michigan, 2014.

[7] J. R. Brophy, L. Friedman, and F. Culick, "Asteroid retrieval feasibility," in *IEEE Aerospace Conference Proceedings*, 2012.

[8] B. Welander, C. Carpenter, K. H. de Grys, R. R. Hofer, T. M. Randolph, and D. H. Manzella, "Life and Operating Range Extension of the BPT-4000 Qualification Model Hall Thruster," in *AIAA/ASME/SAE/ASEE Joint Propulsion Conference & Exhibit*, 2006, vol. 42, p. 5.

[9] R. Liang, "The Combination of Two Concentric Discharge Channels into a Nested Hall-Effect Thruster," University of Michigan, 2013.

[10] J. M. Haas and A. D. Gallimore, "Considerations on the Role of the Hall Current in a Laboratory-Model Thruster," in *37th Joint Propulsion Conference*, 2001, no. July, p. AIAA 2001–3507.

[11] J. A. Linnell and A. D. Gallimore2, "Hall Thruster Electron Motion Characterization Based on Internal Probe Measurements," *31st International Electric Propulsion Conference*. 2009.

[12] C. A. Thomas, N. Gascon, and M. A. Cappelli, "Nonintrusive characterization of the azimuthal drift current in a coaxial ExB discharge plasma," *Phys. Rev. E - Stat. Nonlinear, Soft Matter Phys.*, vol. 74, no. 5, 2006.

[13] a. N. Ermilov, V. F. Eroshenkov, D. N. Novichkov, Y. a. Kovalenko, T. M. Sapronova, T. V. Chernyshev, and a. P. Shumilin, "Oscillations of the Hall current in a Hall thruster with an anode layer," *High Temp.*, vol. 52, no. 3, pp. 360–365, Jun. 2014.

[14] A. I. Bugrova, V. S. Versotskii, and V. K. Kharchevnikov, "Determination of the Radial Center of Gravity of an Azimuthal Drift Current in Accelerators with Closed Electron Drift," *Sov. Phys.*, 1980.

[15] V. N. Dem'yanenko, I. P. Zubkov, S. V. Lebedev, and A. I. Morozov, "Induction Method for Measuring the Azimuthal Drift Current in a Hall-current Accelerator," *Sov. Phys.*, 1978.

[16] B. Jorns, D. M. Goebel, and R. R. Hofer, "Plasma Perturbations in High-Speed Probing of Hall Thruster Discharge Chambers: Quantification and Mitigation," in *51st AIAA/SAE/ASEE Joint Propulsion Conference*, American Institute of Aeronautics and Astronautics, 2015.

[17] R. Binyamin, "Analysis and Numerical Experimentation of Onboard Diagnostic Systems for Hall Thrusters," Israel Institute of Technology, 2006.

[18] R. A. Martinez, C. R. Mullins, J. Moritz, J. D. Williams, and C. C. Farnell, "Performance Evaluation of a 1.5 kW Hall Effect Thruster with a Center Mounted Heaterless Hollow Cathode Using Xenon and Krypton Propellant," in *62nd JANNAF Propulsion Meeting*, 2015.

[19] M. D. Cubells, C. Reig, A. De Marcellis, A. Roldan, J. B. Roldan, S. Cardoso, and P. P. Freitas, "Magnetic Tunnel Junction (MTJ) sensors for integrated circuits (IC) electric current measurement," in *IEEE SENSORS 2013 - Proceedings*, 2013.

[20] S. Łęski, K. H. Pettersen, B. Tunstall, G. T. Einevoll, J. Gigg, and D. K. Wójcik, "Inverse current source density method in two dimensions: Inferring neural activation from multielectrode recordings," *Neuroinformatics*, vol. 9, no. 4, pp. 401–425, 2011.

[21] H. Saotome and Y. Saito, "Locally orthogonal coordinate systems for analyzing inverse problems of magnetostatic fields: applications to magnetocardiogram and magnetoencephalogram," *IEEE Trans. Magn.*, vol. 29, no. 6 pt 2, pp. 3343–3345, 1993.

[22] M. Yan, S. Udpa, S. Mandayam, Y. Sun, P. Sacks, and W. Lord, "Solution of inverse problems in electromagnetic NDE using finite element methods," *IEEE Trans. Magn.*, vol. 34, no. 5, 1998.

[23] O. Chadebec, J. L. Coulomb, J. P. Bongiraud, G. Cauffet, and P. Le Thiec, "Recent improvements for solving inverse magnetostatic problem applied to thin shells," in *IEEE Transactions on Magnetics*, 2002, vol. 38, no. 2 I, pp. 1005–1008.

[24] J. Weese, “A reliable and fast method for the solution of Fredhol integral equations of the first kind based on Tikhonov regularization,” *Computer Physics Communications*, vol. 69, no. 1. pp. 99–111, 1992.

[25] P. C. Hansen and D. P. O’Leary, “The Use of the L-Curve in the Regularization of Discrete Ill-Posed Problems,” *SIAM Journal on Scientific Computing*, vol. 14, no. 6. pp. 1487–1503, 1993.

[26] Z. Morozko, “Feasability Assessment of Magnetic Sensors for Measurement of Hall Current Induced Changes to the Static Magnetic Field Nearby Hall Thrusters,” 2013.

[27] Micromagnetics, “MTJ 240 Manual.” [Online]. Available: http://www.micromagnetics.com/docs/STJ-240_datasheet.pdf.

[28] S. J. Shah, “Instruments Field Wiring and Noise Considerations for Analog Signals,” pp. 1–27, 1994.

[29] A. Input, “Ni 6366/6368,” vol. 6366.

[30] K. G. Xu and M. L. R. Walker, “High-power, null-type, inverted pendulum thrust stand,” *Rev. Sci. Instrum.*, vol. 80, no. 5, pp. 1–6, 2009.

[31] B. R. Tartler, “Construction and Performance of an Inverted Pendulum Thrust Balance,” Massachusetts Institute of Technology, 2010.

[32] A. D. Kodys, R. Murray, L. Cassady, and E. Y. Choueiri, “An Inverted-Pendulum Thrust Stand for High-Power Electric Thrusters,” in *AIAA/ASME/SAE/ASEE Joint Propulsion Conference & Exhibit*, 2006, vol. 42, no. July, pp. 1–14.

[33] T. Moeller and K. A. Polzin, “Thrust stand for vertically oriented electric propulsion performance evaluation,” *Rev. Sci. Instrum.*, vol. 81, no. 11, 2010.

[34] K. Polzin, T. E. Markusic, B. J. Stanojev, A. Dehoyos, and B. Spaun, “Thrust stand for electric propulsion performance evaluation,” in *Review of Scientific Instruments*, 2006, vol. 77, no. 10, pp. 1–10.

[35] A. N. Grubišić and S. B. Gabriel, “Development of an indirect counterbalanced pendulum optical-lever thrust balance for micro- to millinewton thrust measurement,” *Measurement Science and Technology*, vol. 21, no. 10. p. 105101, 2010.

[36] J. Polk, A. Pancotti, T. Haag, S. King, and M. Walker, “Recommended Practices in Thrust Measurements,” in *33rd International Electric Propulsion Conference*, 2013, pp. 1–24.

[37] C. A. Thomas, N. Gascon, and M. A. Cappelli, “AIAA 2003-4854 A Study of the Azimuthal Electron Drift in an E × B Discharge Using a Non-invasive Antenna Array,” no. July, pp. 1–8, 2003.

[38] J. F. Ogilvie, “A monte-carlo approach to error propagation,” *Comput. Chem.*, vol. 8, pp. 205–207, 1984.

[39] D. Liu, “Two-Dimensional Time-Dependent Plasma Structures of a Hall Effect Thruster,” Air Force Institute of Technology, 2011.